Theory of Terahertz generation by Optical Rectification

by

Koustuban Ravi

B.Eng., Nanyang Technological University (2009)

Submitted to the Department of Electrical Engineering and Computer Science

in partial fulfillment of the requirements for the degree of

Master of Science in Electrical Engineering and Computer Science

at the

MASSACHUSETTS INSTITUTE OF TECHNOLOGY

September 2014

Signature redacted

Author.....

Department of Electrical Engineering and Computer Science
August 29 2014

Certified by..... Signature redacted .....

Franz X.Kärtner
Adjunct Professor of Electrical Engineering
Thesis Supervisor

Certified by..... Signature redacted .....

Erich P.Ippen
Elihu Thomson Professor of Electrical Engineering, Professor of Physics Emeritus
Thesis Supervisor

Accepted by..... Signature redacted .....

Leslie A. Kolodziejski
Professor of Electrical Engineering
Chair, Department Committee on Graduate Students

Theory of Terahertz Generation by Optical Rectification

by

Koustuban Ravi

Submitted to the Department of Electrical Engineering and Computer Science on August 29 2014, in partial fulfillment of the requirements for the degree of Master of Science

Abstract

Intense pulses of light with wavelengths approximately ten times smaller than microwave sources and a hundred times larger than optical/near infra-red sources may be categorized as high-field Terahertz (THz) sources. By virtue of their large electromagnetic field amplitudes and relatively long wavelengths, they are uniquely amenable for electron acceleration, coherent X-ray generation and non-linear spectroscopy. Intra-pulse difference frequency generation or optical rectification of ultrafast optical pump pulses in non-linear crystals has emerged as the most efficient approach for high-field THz generation. Earlier theoretical treatment of these systems had predicted conversion efficiencies as high as 10%, which opened up the possibility of generating THz pulses with energies on the order of 10 milli joules on a table-top. However, experimental demonstrations have achieved conversion efficiencies of only a few percent which motivates a re-examination of the existing theory. In this thesis, we re-formulate the problem by accounting for effects, previously not considered. These include: (i) the spatio-temporal distortions of ultrafast pulses, (ii) the nonlinear coupled interaction of optical and THz radiation in two spatial dimensions (2-D), (iii) self-phase modulation, (iv) stimulated Raman scattering and (v) crystal geometry. The key finding is that THz generation necessarily leads to broadening of the optical pump spectrum, resulting in a rapid spatio-temporal break-up of the pulse which limits further generation of THz radiation. Due to this self-limiting mechanism, the predicted conversion efficiencies reduce significantly in relation to earlier predictions, which is in line with experimental trends. Guidelines to optimize conversion efficiency and their ramifications on spatial and spectral properties of THz radiation are discussed. The predictions and analyses are supported by experiments. These findings direct future work towards careful engineering of such systems to achieve optimal THz pulse properties and the conception of approaches to circumvent the aforementioned self-limiting effects.

Thesis Supervisor: Franz X.Kärtner
Title: Adjunct Professor of Electrical Engineering

Thesis Supervisor: Erich P.Ippen
Title: Elihu Thomson Professor of Electrical Engineering, Professor of Physics Emeritus
Thesis Supervisor

Acknowledgment

I have had an incredible time at MIT over the course of the last two years. It is perhaps a cliché to state that this place is special but one cannot emphasize sufficiently, how true this is. While much work needs to be done to meet the institute's standards, it is befitting that I acknowledge those who have played a role in my relative success (**or more accurately, the lack of it**) so far.

First, I would like to thank **Prof. Sheel Aditya** from Nanyang Technological University (NTU) for introducing me to Electromagnetic Theory research, early in my sophomore year during my undergraduate studies. His encouragement played an important role in spurring my scientific aspirations. A key turning point in my career was working with **Prof. Seng-Tiong Ho** from Northwestern University. He had a strong influence on my approach to solving problems, writing methodology and research philosophy. The training I received from him was a key reason for me being able to conduct research independently at graduate school. It would be fair to say that I probably would not have been at MIT if not for his unwavering support.

At MIT, I have had numerous individuals to look up to. Among staff in the Optics and Quantum Electronics (OQE) group, I have had good role models in **Billy Putnam, Donnie Keathley and Emilio Nanni**. The first papers I studied in the area of optics and photonics were those of Prof Ippen's and Prof Hermann Haus. I am grateful to have **Prof. Ippen** as my co-advisor. Discussions with him have always given me a fresh perspective on scientific and strategic fronts because of his clarity. On my very first day of class at MIT, I was particularly impressed **by Prof. Hagelstein's** raw intellectual horsepower and hope to match it at some point. I have had interesting conversations with every member of the OQE group – **Damian Schimpf, Gregory Stein, Hung-Wen Chen, Jeffrey Moses, Kyung-Han Hong, Liang-Jie Wong, Patrick Callahan and Siddharth Bhardwaj**. In addition, I would like to thank **Arya Fallahi, Frederike Ahr, Sergio Carbajo and Xiaojun Wu** from DESY in Hamburg for engaging in what promises to be a fruitful collaboration. A special mention to my team mate on the terahertz project – **Wenqian Huang** for useful and important discussions on various fronts. **Peter Krogen** has been a great friend and colleague.

I am fortunate to have **Prof. Franz X. Kärtner** as my advisor. Despite his numerous responsibilities, he unbelievably makes time for discussions. He has given me ample freedom but also intervened at the right times to ensure things stay on course. His broad scientific repertoire was a key reason which drew me to the group but the most important pieces of knowledge that I have derived from Franz have been outside the technical realm. His pleasant demeanor, patience, optimism and outstanding leadership skills are truly worth emulating and have influenced me deeply.

Prof. Martin A. Schmidt, has promptly provided counsel whenever sought, in his capacity as my graduate mentor.

I cannot thank my parents – **Mohana Ravi and Ravi Gopalan** enough for their herculean efforts in raising, educating me and my brother - **Ramgopal Ravi** for exposing gaps in my perception and entertaining me.

Contents

List of Figures

1. Introduction

1.1 Motivation

To set this thesis into context, it is instructive to describe the ultimate goal at the outset which is the development of a table-top source of coherent X-ray pulses. The first question then is perhaps why coherent X-rays? First, short bursts of coherent X-rays can be used to study a number of scientific phenomena, previously not possible. A large number of reactions in chemistry and biology occur at extremely short timescales (ultrafast processes). Currently, these reactions are studied with optical spectroscopic techniques, which obfuscate many of the finer details of the science governing these processes. A coherent X-ray source would enable study of such systems with unprecedented detail [1] – with atomic spatial resolution and unravel important details about various energy conversion processes. One example is the study of photosynthesis, a deeper understanding of which will have important implications on the long term solution to the societal energy problem.

In addition, coherent X-rays would open up the possibility of clinical phase-contrast imaging using X-rays. Current X-ray imaging modalities employ incoherent X-rays and use their attenuation as the contrast mechanism. This limits visualization of features with similar attenuation (e.g. tumors and surrounding soft tissue). With coherent X-rays, the phase alteration imparted by tissue can be measured instead, since phase differences in different soft tissues are ~1000X greater than their attenuation differences. Initial experiments show that phase contrast can for the first time, distinguish normal from cancerous tissue, characterize components of atherosclerotic plaque (the main culprit behind heart attacks and strokes) and show soft tissue anatomy with detail unrivalled by any existing imaging modality. Accurate diagnosis is therefore expected to have a huge impact since cardiovascular disease and strokes alone incur ~300 billion US dollars [2] while cancer incurs 228 billion US dollars in the US annually. Radiation therapy using hard X-rays is another important problem that can benefit from a coherent X-ray source. Current therapy using incoherent X-rays are limited in their ability to localize radiation to the region to be treated which leads to unwanted side effects due to radiation dose to neighboring tissues. With a coherent source of hard X-rays, it would be possible to generate a highly accurate radiation therapy plan for highly localized treatment.

Next we ask, how does one achieve this target? As always, multiple approaches exist. Higher harmonic generation (HHG) is currently the most widely pursued approach but has low conversion efficiencies between 10^{-9} and 10^{-12}. It therefore makes sense to look for alternative approaches, since existing approaches have not yielded significant returns over several years. An alternative approach, with potential to achieve conversion efficiencies of 10^{-4}, is to create a bunch of coherently accelerated electrons, with many Giga electron-volt of energy (GeV) and then decelerate them coherently, all at the same time to create a source of coherent X-rays. The acceleration would have to be especially compact for this approach to be feasible. Typically, accelerating electrons up to a 10 GeV using current radio frequency

based linear accelerators (LINACS) would require a distance in the kilometer (km) range. If, the size of such structures can be shrunk by a factor of 100, to ~10m, it would be possible to house them in laboratories or clinics. Such compact electron sources in themselves are extremely useful for a number of applications – once again in the areas of medicine (skin therapy [3]), imaging and scientific investigation [4].Therefore in addition to the goal of generating coherent X-rays, there are other short term rewards to be reaped.

The current RF sources with wavelengths of a few tens of cm have low peak electric fields, which prevents them from imparting a strong force to the electron. Consequently, a long distance on the order of ~kilometers (km) is necessary for accelerating electrons upto a several GeV of energy. Using intense electric fields of optical pulses is one way to accelerate electrons over very short distances. However, since the optical wavelength is very short (~ μm), the slow –moving electron lags the electric field of the fast propagating light and is likely to experience an equally powerful retardation due to the negative half-cycle of the optical electric field. Therefore, while the force the electron experiences is very large, the acceleration is not very efficient because of the short wavelength of the optical field.

Wavelengths, approximately 100 times smaller than RF and a hundred times larger than optical radiation, could serve as a sweet spot for accelerating electrons by leveraging on the relative advantages of both kinds of radiation- long wavelengths similar to RF radiation and large electric fields similar to optical radiation. Theoretical calculations [5] reveal that acceleration of electrons from rest to 10 MeV energy levels would require radiation at ~500 μm with 10 mJ pulse energy and pulse duration tunable in the range of a few ps (for acceleration from rest to the MeV or relativistic level) to a few hundred ps (for acceleration from the MeV to GeV level). This would result in Giga-Watt (GW) peak powers and peak electric fields in the GV/m range or higher. This region of the electromagnetic spectrum with wavelengths between 3 mm (100 GHz) and 3 μm (10,000 GHz) is generally defined to be the terahertz (THz) region of the electromagnetic spectrum. Once again, a source of THz radiation with 10 mJ pulse energy and a GW of power in itself has many rich applications. The most relevant area is that of nonlinear spectroscopy – i.e, the investigation of the properties of a number of different molecular and solid-state materials [6].

1.2 Reviewing various THz generation methods

Initially, considered a 'forbidden zone' due to its location at the extremities where both electronic and optical technologies reach their limits, a number of continuous wave (CW) and pulsed THz sources have been developed to fill the so called 'THz gap'. It is worthwhile to examine these various technologies in order to ascertain which approach would enable us to get to the goal of 10 mJ pulse energy with pulse durations in the few to hundred picosecond range and intense electric fields.

One broad category of CW sources comprises of solid-state devices which up-convert frequency [7]- [8]. Such sources produce radiation in the lower range of THz frequencies (0.1 to 1 THz). Quantum Cascade Lasers (QCL's) form another important category of CW THz sources, predominantly for higher THz frequencies (1-10 THz) [9]. Solid-state photomixers are the most commercially ubiquitous technology and can produce broadband THz pulses (~ ps duration) as well as CW radiation in the (0.1 to 3 THz) range [7]. However, the above sources are limited to low THz peak fields and cannot be scaled to the desired 10 mJ level pulse energies.

Other sources of THz radiation are vacuum electronic devices (VED's) [10] which can produce peak output powers anywhere from a kW to a GW (free-electron-lasers). However, output from VED's tend to be at the lower THz frequency range of ~ 0.1 THz. While, travelling wave tubes can reach higher THz frequencies, they are limited in bandwidth (a few nanoseconds of pulse duration) and peak powers (MW). Free-electron lasers produce radiation with the desired properties but are expensive, inaccessible and not amenable for deployment in conventional research laboratories.

Down-conversion of optical frequencies using nonlinear optical crystals has emerged as a potential approach to generating THz pulses with peak powers, bandwidths and fields in the desired range. The feasibility of the approach is enabled by the development of relatively cost-effective and robust table-top solid-state laser technology, producing upto 100 mJ pulse energies at kHz repetition rates in the optical/ infrared (IR) spectral region.

A number of crystals – gallium arsenide, gallium phosphide, zinc telluride, cadmium sulphide, lithium niobate and organic crystals – DAST/DSTMS [11] are potential candidates for crystals in such non-linear down conversion processes. However, nonlinear absorption processes in various crystals impose specific requirements of the optical pump wavelength. Of various solid-state laser technologies, lasers centered at 800 nm or 1 μm are the most mature and therefore it makes sense to exploit these advancements for THz generation. An important material system amenable to pumping by these wavelengths is lithium niobate. It also possesses amongst the highest second order nonlinear susceptibility values.

Of various nonlinear optics based approaches, optical rectification (OR) or intra-pulse difference frequency generation (DFG) using tilted-pulse-fronts in lithium niobate has emerged as the most efficient approach [12]- [13]. Optical-to-THz conversion efficiencies in excess of 1% [14], THz pulse energies of 0.4mJ [15] have been demonstrated. These promising initial results have attracted significant interest in further scaling of the approach. In addition, theoretical calculations predict further improvements to conversion efficiency and pulse energies [16].

1.3 Considerations for the formulation of an accurate Theory

Theoretically, up to 10% conversion efficiency has been predicted for the above approach [16]. This translates to THz pulses with pulse energies of 10 mJ or peak powers of several GW. However, experimental demonstrations have only produced conversion efficiencies of a few percent at best, despite the use of theoretically prescribed conditions. The significant gap between theory and experiment poses important questions about why the demonstrated efficiencies are much lower than expected and suggests a possible gap in the current level of understanding of the approach. Therefore, a re-examination of existing theory is warranted.

A few key physical effects have to be included for satisfactory modeling of THz generation via optical rectification using tilted-pulse-fronts. These effects have been omitted in the present models in the literature.

(i) In optical rectification using tilted-pulse-fronts, an optical pump pulse is angularly dispersed to produce an intensity front which is tilted with respect to its propagation direction. The generated THz radiation propagates perpendicular to this tilted intensity front or tilted-pulse-

front. Since the optical and THz radiation travel different distances in the same time, the large difference between optical and THz refractive indices is compensated and phase matching is achieved. As a consequence of the angular dispersion of the optical pump pulse, various frequency components of the optical pump pulse spectrum are now spatially separated and have different amplitudes and phases at each spatial location. This is tantamount to having different spectral bandwidths and pulse durations at each spatial location. These *spatio-temporal distortions* of the optical pump pulse are expected to affect the properties of the generated THz radiation and have to be accounted for.

(ii) Since the generated THz propagates perpendicular to the tilted-pulse-front, the optical pump and THz radiation propagate non-collinearly in different directions. Therefore, the problem can only be satisfactorily described in a minimum of two spatial dimensions (2-D).

(iii) As THz radiation is generated, it is accompanied by a dramatic cascaded frequency down-shift and spectral broadening of the optical pump pulse spectrum (*cascading effects*) which has been experimentally modelled but not satisfactorily modelled in theory. While the optical pump energy is relatively undepleted due to small conversion efficiencies, the spectral re-shaping is drastic and therefore expected to play a role.

(iv) At very high intensities, in addition to cascading effects, *self-phase-modulation* maybe an important factor and would have to be modelled.

A comprehensive theoretical model should therefore be able to account for all of the above effects. This would require a simultaneous solution of optical and THz electric fields (henceforth referred to as field) in at least two spatial dimensions (2-D). In addition, spatio-temporal distortions imparted by the imaging optics should also be considered.

Previously presented models broadly comprise of (i) 1-D and 2-D spatial models without the inclusion of cascading effects and (ii) 1-D spatial models which account for cascading effects. Of works in the first category, a one-dimensional (1-D) spatial model including the effects of material dispersion and group velocity dispersion due to angular dispersion (GVD-AD) was presented [17]. It included a Drude model for free-carrier-absorption (FCA) of THz radiation to account for the saturation of THz energy. In [18], a 1-D model considering material dispersion, GVD-AD and self-phase modulation (SPM) was presented. In [19], a 2-D model which took into account material dispersion, GVD-AD and crystal geometry was developed. In the second category, an effective 1-D model with cascading effects was first presented in [20] and improved in [21]- [22].None of the presented models include the effects of spatio-temporal distortion of the optical pump pulses or cascading effects in 2-D.

1.4 Description of thesis

In Chapter 2 of this thesis, we motivate the need for the development of a comprehensive theory, by illustrating the physics at work in optical rectification using tilted-pulse-fronts.

Chapter 3, initiates the reader to THz generation by optical rectification using tilted-pulse-fronts by simple models with undepleted pump approximations. Simple analytic expressions are derived which bring out certain essential features of the model. These include the nature of the generated THz spectrum, the effects of dispersion and absorption. The chapter ends with a discussion on its failure to account for the saturation of conversion efficiency, which is experimentally observed.

In Chapter 4, we solve simultaneously for both optical and THz fields. We show that the experimentally observed cascaded frequency down-shift and spectral broadening is a direct consequence of THz generation. It is shown that this spectral broadening accentuates dispersive effects and ultimately limits further THz generation. This is an important finding in that it indicates that optical rectification using titled-pulse-fronts is a self-limiting process. The contents of this chapter also constitute a journal publication.

In Chapter 5 of this thesis, we present a detailed formulation of the model which simultaneously accounts for spatio-temporal distortions of the optical pump pulse, cascading effects, SPM and Stimulated Raman Scattering (SRS) effects, material dispersion and absorption as well as nonlinear crystal geometry in 2-D. We validate the model by comparisons to theory and experiment and provide guidelines on how to optimize the experiment for conversion efficiency. We find that the increase in conversion efficiency is not always desirable as other properties such as beam quality are also affected. This lays the foundation for more careful optimization of THz sources based on optical rectification.

We conclude in Chapter 6, laying the roadmap for future work.

2. Physical description of the problem and general approach

In this chapter, we provide an overview of the physics at work in optical rectification using tilted-pulse-fronts. This should serve to motivate the theoretical development of the remainder of the thesis. The overall schematic of our approach is depicted in Fig. 2-1(a). An optical pump pulse with input electric field described by $E_{op}^{in}(\omega, x_0, z_0)$ at angular frequency ω, propagating in the z_0 direction is incident on an arbitrary setup for creating tilted-pulse-fronts. The co-ordinate axes x_0 and z_0 are as depicted in Fig. 2-1(a). In Fig. 2-1(a), electric fields at only two angular frequencies $-\omega$ and $\omega+\Omega$ are depicted for convenience although there are an infinitely large number of frequency components in the optical pump pulse spectrum. The tilted-pulse-front setup can be chosen arbitrarily could include a grating and lens, a grating and a telescope, a contact grating etc. The most commonly employed setup for generating tilted-pulse-fronts is comprised of a diffraction grating and a single lens and is depicted in Fig. 2-1(b).

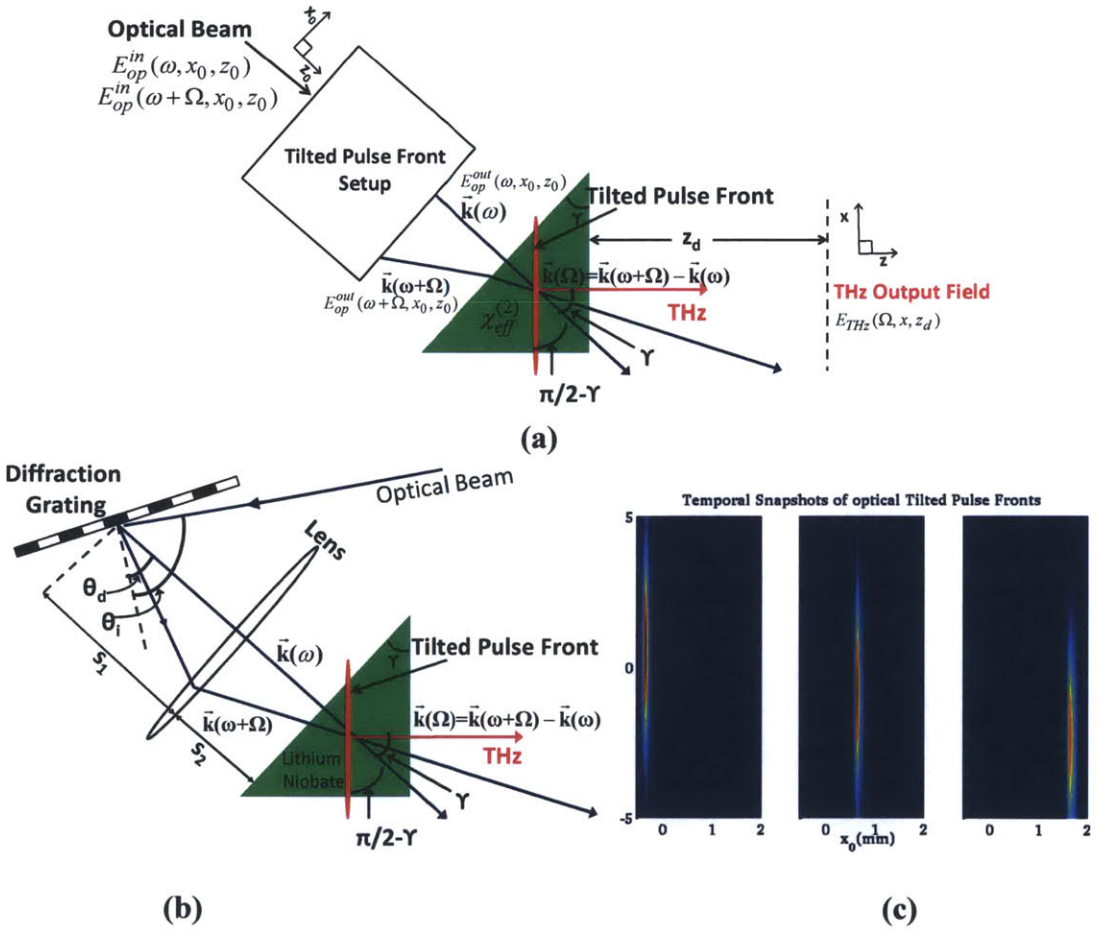

Figure 2-1 : (a) An optical pump pulse with phasor $E_{op}^{in}(\omega, x_0, z_0)$ is incident on an arbitrary setup to generate a tilted-pulse-front. The angular dispersion of various spectral components can generate THz radiation inside the nonlinear crystal via optical rectification by satisfying the appropriate phase-matching condition. From a time-domain viewpoint, the angularly dispersed pulse forms a tilted-pulse-front as shown by the red ellipse. THz radiation is generated perpendicular to this tilted-pulse-front. (b) The most common setup used for tilted-pulse-front optical rectification is a combination of a diffraction grating and lens (c) Time domain snapshots of tilted-pulse-fronts in the

(x-z) co-ordinate system from Fig. 2-1(a). The intensity-fronts are parallel to the output facet but the propagation direction is oblique to this.

The optical pump pulse is incident at an angle θ_i with respect to the normal of the grating surface and each frequency component of the optical pump pulse with angular frequency ω scatters off at a different angle $\theta_d(\omega)$. A focusing lens, located at a distance s_1 from the diffracting grating is used to image this angularly dispersed optical pump pulse onto the lithium niobate crystal located at a distance s_2 from the lens as shown in Fig. 2-1(b). An optical pulse with a tilted-pulse-front is typically angularly dispersed [23]. Therefore, various frequency components of the emergent optical field described by the phasor $E_{op}^{out}(\omega, x_0, z_0)$ propagate at different angles. This is depicted in Fig. 2-1(a)-(b) as the spectral components at ω and $\omega+\Omega$ emerge with corresponding wave vectors $\vec{k}(\omega), \vec{k}(\omega+\Omega)$ respectively. Since optical rectification is essentially difference frequency generation (DFG), in the phase matched condition, the propagation vector of the generated THz (at angular frequency Ω) is given by $\vec{k}(\Omega) = \vec{k}(\omega+\Omega) - \vec{k}(\omega)$ as seen in Fig. 2-1(a)-(b). The generated THz then emerges at an angle γ with respect to the direction of propagation of the optical pump pulse and exits approximately normal to the output facet of the crystal.

In the time domain, such an angularly dispersed pulse has an intensity profile which is tilted with respect to its propagation direction as delineated by the red ellipse in Fig. 2-1(a) which gives rise to the terminology of 'tilted-pulse-front'. This red ellipse makes an angle $\pi/2-\gamma$ with respect to the propagation direction of the optical pulse, where γ is referred to as the pulse-front-tilt angle. This is depicted via temporal snapshots of the intensity profile of an angularly dispersed optical pulse in Fig. 2-1(c), where the pulse propagates obliquely but has an intensity profile parallel to the output facet. A theoretical description of tilted-pulse-fronts and their relationship to angular dispersion is provided in Appendix A.

Since, the various frequency components are angularly separated, they have separating field profiles which leads to a spatial variation in the average frequency as well as relative amplitude and phase across the beam profile. As a consequence, the pulse durations and bandwidths at various points in space are different, which in turn has implications on the spatial properties of the generated THz pulse. These spatial variations of frequency and pulse duration as a consequence of angular dispersion and spatial chirp are categorized as spatio-temporal variations. In Chapter 5, we consider these spatio-temporal effects by applying an analytic formulation of dispersive ray pulse matrices [24]. This approach efficiently models the various spatio-temporal effects associated with the optical pulse for an arbitrary tilted-pulse-front setup and supplies $E_{op}^{out}(\omega, x_0, z_0)$ at the input face of the nonlinear crystal. In chapter 5, this is then used as an initial condition for the solution of a system of 2-D coupled nonlinear wave equations in the nonlinear crystal to obtain both THz and optical field profiles.

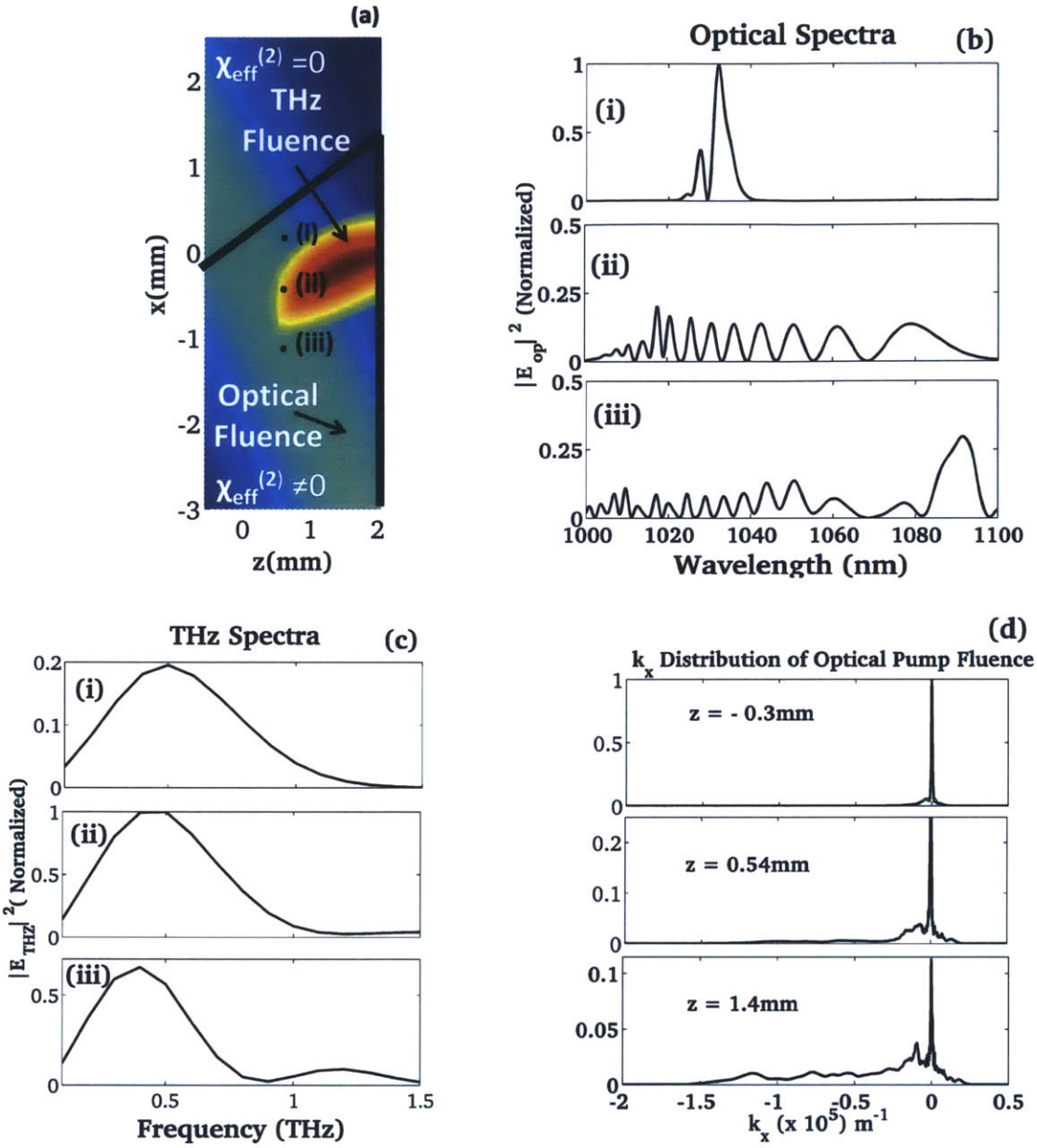

Figure 2-2 (a). Spatial distribution of the optical and THz fluences. The THz field propagates in the z direction with the optical field at an angle γ with respect to it. THz is only generated over a small portion of the optical field due to spectral broadening of the optical pulse by cascading which results in phase mismatch for subsequent portions of the beam (b) Optical spectrum is broadened between (i)-(iii) due to cascading effects. (c) THz spectra at locations (i)-(iii) shows significant spatial-chirp. (d) Since each frequency component has a certain value of transverse momentum, spectral broadening also necessarily results in broadening in transverse momentum k_x.

In Fig. 2-2, we provide a sample solution of the system of 2-D nonlinear equations using the developed model. Fig. 2-2(a), depicts the optical and THz fluences obtained. Regions within the green lines contain nonlinear material with a non-zero second order susceptibility. In the (x-z) co-ordinate system, the optical pump pulse propagates obliquely in the nonlinear crystal as indicated by the cyan/light-blue regions in Fig. 2-2(a). The THz pulse however propagates in the z direction, at an angle γ to the optical pump pulse and emerges approximately perpendicular to the output face as seen by the THz fluence in red.

As the optical pulse propagates, it generates a THz photon at Ω and simultaneously suffers a frequency downshift by the same amount. Upon each successive generation of a THz photon at Ω, it repeatedly experiences a frequency down-shift or a 'cascaded' frequency down-shift which leads to a large spectral broadening of the optical pump pulse spectrum as seen in Fig. 2-2(b). However, as the optical pump pulse spectrum is modified, the subsequent THz spectrum is also modified as shown in Fig. 2-2(c) and vice-versa. As a result, there is a great spatial variation in both optical and THz spectra as seen in Fig. 2-2(b) and 2-2(c). The spatial-chirp of the THz spectrum has important implications on beam transport and focusing properties. This spatial-chirp in THz and optical spectra has been observed experimentally [25] but not explained theoretically, until now.

For an angularly dispersed pulse, each spectral component of the optical pulse at ω has a well-defined transverse momentum k_x. Therefore, spectral broadening of the optical pulse also leads to a re-distribution of the optical pulse energy among various transverse momentum (k_x) values. Therefore, as the optical pulse propagates, it also broadens in transverse momentum. Eventually, as the optical spectrum is broadened as seen in Fig. 2-2(b), the angular dispersion is accentuated to such a great extent that phase matching is lost and THz generation ceases altogether. This is seen in Fig. 2-2(a) where THz is generated only over a small distance of optical pump pulse propagation. Previous theoretical treatments have ignored this spectral broadening of the optical pump pulse in their calculations which has led to a gross overestimation of the achievable conversion efficiency [16]. This finding has very important implications on the scalability of this approach. This large broadening of the optical pump pulse spectrum causes a temporal break-up of the pulse. Similarly, due to broadening in transverse momentum, there is also a spatial break-up of pulses. In combination, a rapid spatio-temporal break-up of the optical pulse occurs as shown in Fig. 2-3. Thus, different parts of the optical pulse arrive at different time instants and the generated THz no longer builds up coherently. This physical picture, based on the spatio-temporal break-up of pulses due to broadening in transverse momentum and frequency, is a new lens to look at the THz generation process.

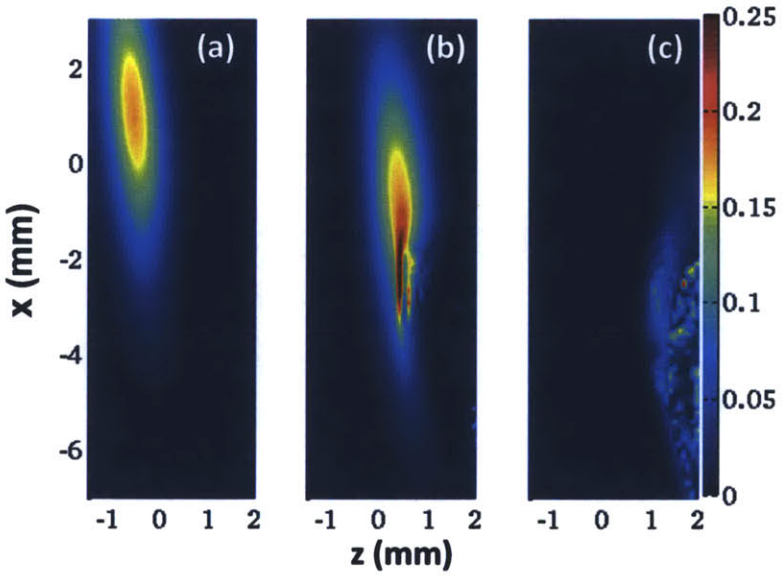

Figure 2-3 : Spatio-temporal break-up of the optical pulses due to simultaneous broadening in frequency and transverse momentum. Due to spatio-temporal break-up, different parts of the optical pump arrive at different times, preventing further coherent build-up of THz radiation.

Thus, in this thesis, a few important findings are presented. First, it resolves the question as to why THz conversion efficiencies are not as high as predicted. Next, it provides a detailed physical description of the optical rectification process and identifies the rapid spatio-temporal break-up of optical pulses as the key limiting factor to THz generation. This new physical picture has important implications on the scaling of optical pump energies and beam sizes. It also informs us on what factors need to be considered while optimizing the setup.

3. Optical rectification in the undepleted limit

In Chapter 2, we provided an overview of the physics at work in the process of THz generation by optical rectification using tilted-pulse-fronts. In order to build up to the level of understanding required to accurately model such systems, it would be useful to start with models where the undepleted pump approximation is invoked. Since the experimentally observed optical to THz conversion efficiencies (or conversion efficiency for short) are < 10%, this would seem to be a reasonable approximation at first. It will be seen in this section that such models are in fact sufficient to explain many essential features of THz generation by optical rectification, at least qualitatively.

Although THz generation using tilted-pulse-fronts is a non-collinear process and can be modeled satisfactorily only in two dimensions (2-D), we begin with an analysis using an effective 1-D equation, similar to [26]. Let the electric field of THz radiation with angular frequency Ω be z propagating and denoted by $E_{THz}(\Omega, z)$. The optical pump pulse propagates at an angle γ with respect to the THz pulse, where γ is the pulse-front-tilt angle. In order to reduce the problem to a single dimension, it is useful to note that if the THz field propagates a distance z, the optical field propagates a distance z/cosγ or alternatively, the effective wave number of the optical field may be divided by a factor of cosγ. Such a model would be phenomenological, but it is effective in providing an understanding of many of the features of optical rectification using tilted-pulse-fronts.

Keeping in mind the above, we write the 1-D wave equation for the THz electric field at each angular frequency Ω driven by the nonlinear polarization term $P_{THz}(\Omega, z)$.

$$\frac{d^2 E_{THz}(\Omega, z)}{dz^2} + k^2(\Omega) E_{THz}(\Omega, z) = -\frac{\Omega^2}{\varepsilon_0 c^2} P_{THz}(\Omega, z) \tag{3.1}$$

The nonlinear polarization term for THz radiation at an angular frequency Ω for optical rectification is basically an ensemble of all possible difference frequency generation processes within the bandwidth of the optical pump pulse spectrum. Consequently, it may be written down according to (3.2), where $\chi^{(2)}_{eff}$ is the effective second-order nonlinearity of the material.

$$P(\Omega, z) = \varepsilon_0 \chi^{(2)}_{eff} \int_0^\infty A_{op}(\omega + \Omega) A_{op}{}^*(\omega) e^{-j(k(\omega+\Omega)-k(\omega))z} d\omega \tag{3.2}$$

In (3.2), $A_{op}(\omega)$ is the envelope of the electric field of the optical pump pulse at angular frequency ω. The factor in the exponent $k(\omega+\Omega) - k(\omega) = (\cos\gamma)^{-1} \Omega n_g(\omega_0)/c$ when the effects of group velocity dispersion are excluded. It phenomenologically represents the tilted-pulse-front. For a transform-limited Gaussian pulse centered at ω_0, the expression in (3.2) reduces to that in (3.3).

$$P_{THz}(\Omega) = \varepsilon_0 \chi^{(2)}_{eff} \frac{E_0^2 \tau}{2\sqrt{2\pi}} e^{-\frac{\Omega^2 \tau^2}{8}} \tag{3.3a}$$

$$A_{op}(\omega) = \frac{E_0 \tau}{2\sqrt{\pi}} e^{-\frac{\tau^2(\omega-\omega_0)^2}{4}} \tag{3.3b}$$

In (3.3), E_0 is the peak electric field amplitude and $\tau/\sqrt{2}$ is the e^{-2} pulsewidth. It can be related to the full width at half maximum (FWHM) pulse width by the relation $\tau_{FWHM}/\sqrt{2\ln 2} = \tau$. A general analytic solution to (3.1) is possible in the limit that group velocity dispersion (GVD) of the optical pulse is neglected. It is instructive to examine this expression as it provides significant insight into the properties of THz radiation generated via optical rectification. In general, the solution to (3.1) is a sum of a homogeneous solution and a forced solution. This is expressed below in (3.4). The backward propagating THz wave is assumed to be zero. This is a reasonable approximation in sufficiently thick crystals where the backward propagating THz wave would be absorbed by the material.

$$E_{THz}(\Omega, z) = \mathrm{C}e^{-j k(\Omega) z} - \frac{\Omega^2 \chi_{eff}^{(2)} E_0^2 \tau}{c^2 2\sqrt{2\pi}} e^{-\frac{\Omega^2\tau^2}{8}} e^{-j\frac{\Omega n_g(\omega_0)}{c} z} \tag{3.4}$$

The constant C, is resolved by applying the boundary condition $E_{THz}(\Omega, 0) = 0$ which signifies that the THz field is zero at the beginning of the crystal. Including these arguments, we have the following analytic expression for the THz field in (3.5).

$$E_{THz}(\Omega, z) = -j\frac{\Omega^2 \chi_{eff}^{(2)} E_0^2 \tau e^{-\frac{\Omega^2\tau^2}{8}}}{c^2 2\sqrt{2\pi}} \frac{e^{-j\frac{1}{2}\left(\frac{\Omega n(\Omega)}{c} + \frac{\Omega n_g(\omega_0)}{c\cos\gamma}\right) z}}{\left(k(\Omega) + \frac{\Omega n_g(\omega_0)}{c\cos\gamma}\right)} \mathrm{sinc}\left(\frac{\Omega[n(\Omega) - n_g(\omega_0)/\cos\gamma] z}{c}\right) \cdot z \tag{3.5}$$

Equation (3.5) is similar to those from various other nonlinear optical generation processes [27]. Its variation with propagation is characterized by the typical *sinc* function, which is maximum for an argument of zero. This condition dictates the phase-matching condition. Therefore, setting the argument of the *sinc* function in (3.5) to be zero, we obtain the corresponding phase-matching condition in (3.6).

$$n(\Omega)\cos\gamma = n_g(\omega_0) \tag{3.6}$$

This means that the pulse-front-tilt angle γ must be adjusted such that (3.6) is satisfied. In lithium niobate, where the THz refractive index is ~5 and the group refractive index at optical wavelength is ~2.25, the phase-matching angle is ~63 degrees. If this phase-matching condition is satisfied, the THz electric field sees a linear growth with distance. Adopting a time-domain viewpoint, what this means is that as the THz radiation is generated, the optical field propagates at an angle γ to it and the subsequently generated THz radiation adds up coherently with the previously generated THz radiation. In lithium niobate, the dispersion of refractive index in the lower THz range is relatively low and consequently a very broad-band THz pulse is generated. This is the first salient feature of THz generation by optical rectification using tilted-pulse-fronts. We plot the generated THz spectrum and temporal waveform below in Fig 3-1. for a pulsewidth τ_{FWHM} = 750 fs and fluence of 20 mJ/cm^2, propagated over 2 mm. The pulse-front-tilt angle γ was set to ~63^0.

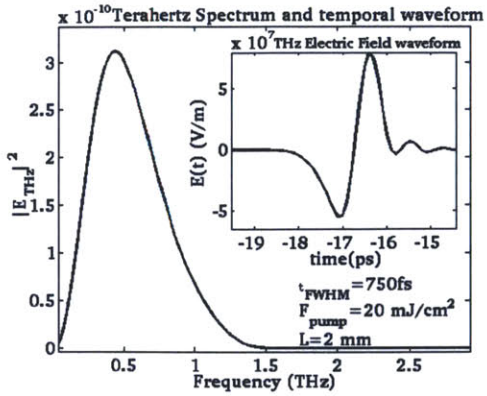

Figure 3-1 : THz spectrum and electric field waveform generated by optical rectification using tilted-pulse-fronts in the phase-matched condition. The pulse-front-tilt angle is $\gamma \sim 63^0$ at 300 K. THz absorption and group velocity dispersion of the optical pulse is neglected. Due to small dispersion of the refractive index in the THz range, a broad band spectrum is generated. The corresponding electric field waveform is an intense 2 ps single-cycle THz pulse with the peak strength on the order of ~MV/cm.

3.1 Effect of tilt angle

One of the key features of tilted-pulse-front phase matching is the high sensitivity of the generation process to the tilt angle of the pulse-front. This sensitivity makes the alignment of the setup critical to both conversion efficiency and the spectral properties of the THz radiation. In the actual experimental setup, γ is controlled by the grating angle and the magnification of the imaging system. Here, we artificially vary it to observe the effects on conversion efficiency as shown in Fig.3-2 (a). The conversion efficiency can be calculated according to (3.7).

$$\eta(z) = \frac{\pi c \varepsilon_0 \int_0^{\infty} n(\Omega) \mid E_{THz}(\Omega, z) \mid^2 d\Omega}{F_{pump}} \tag{3.7}$$

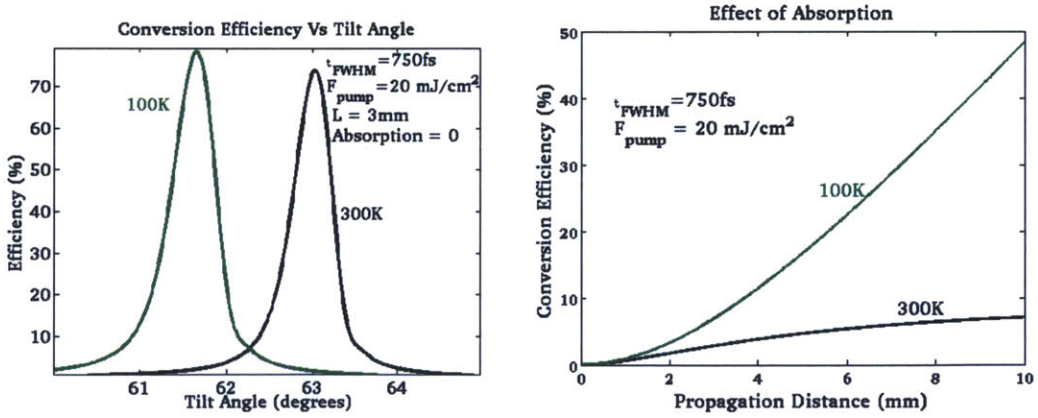

Figure 3-2. (a) Effect of tilt angle on conversion efficiency: Small changes in the tilt angle, can lead to large deviations in the conversion efficiency. This is particularly important while cryogenically cooling the crystal. The refractive index changes must then be compensated by appropriate changes to the setup. Note that the undepleted model is strictly not applicable in the above situations since the conversion efficiencies are very large. (b) Absorption is included into the calculations under phase-matched conditions. The peak efficiencies drop from the 70% level at 300 K to < 10% due to the large absorption of THz radiation at room temperature. After a certain propagation distance, the amount of generated THz saturates. At 100 K, the effects of absorption are alleviated due to a reduction in the absorption coefficient.

3.2 Effect of absorption

If we assume that phase-matching is satisfied in (3.5) but now include an absorption term α_{THz}, then (3.5) reduces to (3.8a). In the presence of some phase mismatch Δk, the general expression for the field is given by (3.8b) and the corresponding magnitude is given by (3.8c).

$$E_{THz}(\Omega,z) = -\frac{\Omega^2 \chi_{eff}^{(2)} E_0^2 \tau e^{-\frac{\Omega^2\tau^2}{8}}}{c^2 2\sqrt{2\pi}} \frac{1-e^{-\alpha_{THz}L/2}}{\alpha_{THz} k(\Omega)} e^{-ik(\Omega)z} \tag{3.8a}$$

$$E_{THz}(\Omega,z) = -\frac{\Omega^2 \chi_{eff}^{(2)} E_0^2 \tau e^{-\frac{\Omega^2\tau^2}{8}}}{c^2 4\sqrt{2\pi} k(\Omega)} \frac{e^{-i\Delta kz} - e^{-\alpha_{THz}z/2}}{\left(\Delta k^2 + \alpha_{THz}^{\ 2}/4\right)} \left(i\Delta k + \alpha_{THz}/2\right) e^{-ik(\Omega)z} \tag{3.8b}$$

$$\left|E_{THz}(\Omega,z)\right|^2 = \left(\frac{\Omega^2 \chi_{eff}^{(2)} E_0^2 \tau e^{-\frac{\Omega^2\tau^2}{8}}}{c^2 4\sqrt{2\pi} k(\Omega)}\right)^2 \frac{\left(\left[1-e^{-\alpha_{THz}z/2}\right]^2 + 4\sin^2\left(\frac{\Delta kz}{2}\right) e^{-\frac{\alpha_{THz}z}{2}}\right)}{\left(\Delta k^2 + \frac{\alpha_{THz}^{\ 2}}{4}\right)} \tag{3.8c}$$

This is also quite akin to what is observed in various nonlinear optical generation processes, i.e. there is an initial increase in the THz field and subsequent saturation. We see this in Fig.3-2(b) for the 300 K case, when the conversion efficiency saturates at about 8% at z~10 mm. In the phase mismatched case, there is decay in the field over longer distances instead of mere saturation. Intuitively, one can understand this as follows. If the THz generation process is not phase matched, there is a sinusoidal cycling of energy between the optical and THz radiation or on an average, there is no increase in the amount of generated THz radiation. However, if there is no average increase in the amount of generated THz but there is a simultaneous absorption of radiation, there is a net decay of THz energy. This is seen in (3.8c) by the presence of the $\sin^2(\Delta kz/2)e^{-\frac{\alpha_{THz}z}{2}}$ term in (3.8c). A solution to mitigate the effects of absorption is to cryogenically cool the lithium niobate crystal to 100 K. This reduces the absorption coefficient and in principle, increases the distance over which THz radiation can be generated as seen in Fig. 3-2(b). However, care must also be taken to realign the setup to introduce the correct pulse-front-tilt angle, since the refractive index of the crystal is sensitive to temperature as seen in Fig. 3-2(a).

3.3 Effect of group velocity dispersion of the optical pulse

In the expression in (3.5), we did not consider the effects of group-velocity dispersion of the optical pulse on the THz generation process. Under this assumption, there is no distortion to either the optical pulse spectrum or the temporal profile as it generates THz radiation. However, since the pulse has a tilted-front, it suffers group velocity dispersion due to both angular and material dispersion. Incidentally, for lithium niobate, angular dispersion is significantly more important by a factor of more than 15. In the presence of such dispersion, the peak intensity of the pulse drops as the pulse broadens in time during its passage through the crystal. The drop in intensity is accompanied by a drop in THz generation. The generated THz is in turn absorbed, leading to decay in conversion efficiency. In addition, due to dispersion, there is a walk-off between the generated THz and optical pump pulses, which leads to a reduction in the coherent build-up of THz radiation (even in the absence of absorption). In the absence of absorption, an analytic expression for the generated THz electric field can be derived for a given group velocity dispersion value

β'' in (3.9). An analytic expression for group velocity dispersion due to angular dispersion can be derived in (3.9b). The derivation of the expression is presented in Appendix A.

$$E_{THz}(\Omega, z) = -j\frac{\Omega\chi_{eff}^{(2)} E_0^2 \tau^2 e^{-\frac{\Omega^2\tau^2}{8}}}{8k(\Omega)c^2|\beta''|} erf\left(\frac{\Omega|\beta''|}{\tau\sqrt{2}} z\right) \tag{3.9a}$$

$$|\beta''| = \frac{n_g^2(\omega_0)\tan^2\gamma}{\omega_0 c n_{op}(\omega_0)} \tag{3.9b}$$

The error function in (3.9a) $erf(x)$, tends to 1 as x tends to infinity. This means that there will be a saturation of the conversion efficiency for large z. Furthermore, the larger the β'', the smaller the value of z at which this saturation occurs is shorter. Similarly, the larger the bandwidth (or shorter the value of τ) the earlier saturation of conversion efficiency sets in. We see these effects in Fig. 3-3(a).

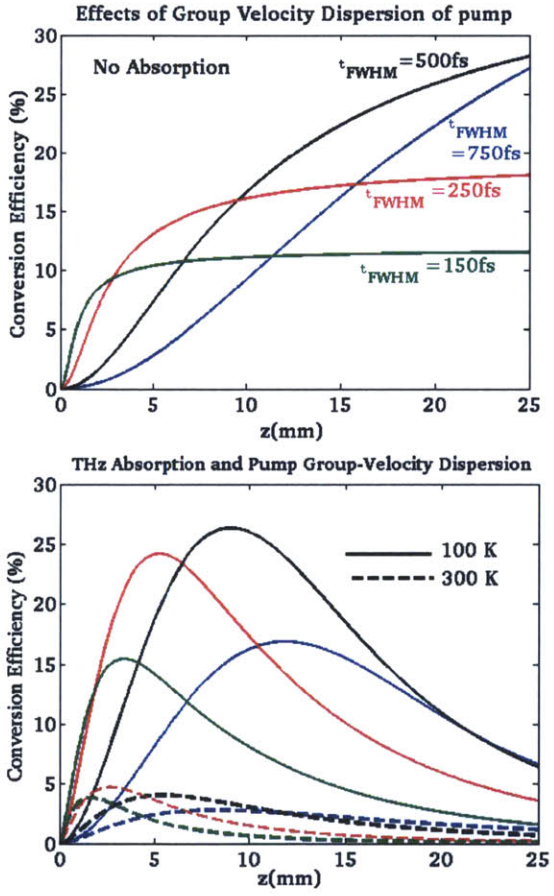

Figure 3-3(a) Effects of group velocity dispersion of the optical pump pulse: In the absence of absorption, the reduction in peak intensity of the pulse leads to a saturation of the conversion efficiency. The saturation occurs at shorter distances for larger bandwidths or larger values of group-velocity dispersion. (b) Numerical solution of (3.1), in the presence of absorption, there is also a decay of conversion efficiency with distance, which is larger for larger temperatures. This is because as the intensity reduces due to dispersion, absorption begins to dominate, leading to a reduction of conversion efficiency.

In Fig. 3-3(b), a numerical solution of (3.1) is presented, taking into account the complete dispersion of refractive index at both optical and THz refractive frequencies as well as angular dispersion. It is seen that inclusion of absorption leads to a drop in conversion efficiencies to the sub -10% level at 300 K.

Furthermore, there is a decay of conversion efficiency with propagation as no further THz is generated due to the drop in intensity of the optical pulse. Consequently, absorption begins to dominate.

3.4 Effect of optical pump intensity

From (3.1) to (3.9), it can be seen that there is no provision in the presented theory describing the limitations to the optical pump intensity. This does not make physical sense, since an arbitrarily high intensity can then be used to convert all the optical energy to THz energy in a short propagation length (where absorption has a minimal impact). In practice, self-phase modulation and associated self-focusing effects as well as optically induced damage present limitations. The limitations to THz conversion efficiency will be studied in detail in the subsequent chapter.

3.5 Summary

An analytic approach was used to illustrate certain key effects associated with THz generation by optical rectification using tilted-pulse-fronts. The phase-matching condition was established and the effects of dispersion and absorption were discussed. However, the model does not account for the saturation of THz generation with increasing optical intensity. Based on the calculations presented above, it would seem that conversion efficiencies in excess of 10% are easily achievable. However, in practice the maximum conversion efficiencies that have been obtained with such systems are an order of magnitude lower (closer to 1%). Furthermore, experimentally a drastic spectral re-shaping of the optical pump pulse is seen which may have implications on the properties of the system. These shortcomings of the model are investigated in the subsequent chapters in greater detail.

4. Limitations to THz generation by optical rectification

In Chapter 3, we used undepleted models to illustrate certain important characteristics of THz radiation generated via optical rectification using tilted-pulse-fronts. A key problem with that theory was that it does not account for the saturation of THz energy. Therefore, conversion efficiencies of 10% or more at 100K are predicted for transform limited 500 fs full-width-at-half-maximum (FWHM) pulses centered at a wavelength of ~ 1 μm using such models [16]. On the other hand, experimental results [14], [28] have not yielded similar values. The disparity between experimental and theoretical results motivates a re-examination of existing models to identify potential shortcomings in theory.

In previous models [17]- [19], the spectral re-shaping of the optical pump pulse caused by THz generation was not considered. However, these effects have to be included to explain the dramatic experimentally observed frequency down-shift and spectral broadening of the optical pump pulse, commensurate with the amount of THz generated, using 1μm [14] as well as 800 nm pump sources [25], [29]. This spectral broadening can intuitively be understood to be a consequence of a cascaded down-shift of the optical pump frequency upon generating THz photons. We will henceforth refer to the cascaded down-shift and spectral broadening of the optical pump pulse spectrum as 'cascading effects'.

In this chapter, we present a 1-D spatial model which does not make an undepleted pump approximation. The model simultaneously accounts for (i) cascading effects, (ii) material and angular dispersion, (iii) absorption, (iv) SPM and (v) stimulated Raman scattering (SRS). The presented model is applicable to simulating a wide variety of OR devices based on different material systems and crystal geometries.

Using the 1-D model, we are able to confirm that the experimentally observed cascading effects are a direct consequence of THz generation. The extent of spectral broadening is demonstrated to be commensurate to the amount of THz generated. Furthermore, in both experiments and theory, it is seen that SPM effects cause negligible spectral broadening. The quantitative agreement of simulated optical spectra and conversion efficiency with experiments [14] is a good validation of the model.

Due to the large spectral broadening resulting from THz generation, the phase mismatch due to dispersive effects is significantly accentuated. Consequently, the conversion efficiency decays much more drastically with propagation length than it would due to other limiting effects such as SPM. Since, GVD-AD (-15000 fs^2/mm) is much larger in magnitude than the group velocity dispersion due to material dispersion at optical frequencies (<1000 fs^2/mm) in lithium niobate, it is the dominant dispersive effect. Therefore, cascading effects in conjunction with GVD-AD represents the strongest limitation to achieving high conversion efficiencies in lithium niobate, especially for pumping at 1 μm (or longer wavelengths). For pumping at 800 nm, in addition to the limitations imposed by cascading effects, it will be shown that FCA is also an impediment to THz generation [29].

We show that neglecting these cascading effects, i.e. the spectral re-shaping of the optical pump spectrum, can lead to a significant overestimation of achievable conversion efficiencies. For example, when cascading effects are excluded, conversion efficiencies as high as 10% have been predicted [16]. However, for similar conditions, the consideration of cascading effects results in conversion efficiencies of only ~2%. Conversion efficiencies at the 1% level are only possible with the greater than 100% optical-to-THz photon conversion levels resulting from cascading effects. However, the spectral

broadening of the optical pump associated with cascading accentuates dispersive effects and strongly limits further increase in conversion efficiency.

4.1 Theory

We first explore the impact of cascading effects using an effective 1-D spatial model. The electric fields corresponding to the optical pulse at spatial co-ordinate z and various angular frequencies ω are denoted by $E_{op}(\omega,z)=A_{op}(\omega,z)e^{-jk(\omega)z}$. The THz electric field at spatial co-ordinate z and angular frequency Ω is denoted by $E_{THz}(\Omega,z)=A_{THz}(\Omega,z)e^{-jk(\Omega)z}$. Here, $A_{op}(\omega,z)$ and $A_{THz}(\Omega,z)$ represent the envelope of the optical and THz fields (henceforth referred to as field) respectively. The wave number for the THz field is given by $k(\Omega)=\Omega n(\Omega)/c$, where c is the speed of light in vacuum. Exact values of the THz refractive index $n(\Omega)$ are used to accurately model the material dispersion in the THz range. The wave number for the optical field is given by (4-1a).

$$k(\omega)=\frac{1}{\cos\gamma}\frac{\omega n(\omega)}{c}+\frac{(\omega-\omega_0)^2}{2}k''(\omega)_{AD} \tag{4-1a}$$

$$k''(\omega)_{AD}=\frac{-n_g^2(\omega_0)}{\omega_0 c n(\omega_0)}\tan^2\gamma \tag{4-1b}$$

Here, the refractive index $n(\omega)$ accounts for material dispersion. The factor $\cos\gamma$ appears in the denominator of the first term in (4-1a) to account for the tilted-pulse-front, where γ is the pulse-front-tilt angle. The second term $k''(\omega)_{AD}$, corresponds to GVD-AD. The expression for GVD-AD is given by (4-1b). The derivation of this expression is provided in Appendix A. In (4-1b), ω_0 is the angular frequency at which the pulse spectrum of the optical pulse is initially centered. The parameter $n_g(\omega_0)$ is the group refractive index of the material at ω_0. Note, that higher order expansion terms can also be derived in (4-1b) but it turns out that they minimally impact the results. When the tilt angle γ=0, (4-1a) reduces to the regular expression for the wave number. Therefore, the developed model can be applied to both non-collinear and collinear OR geometries. The evolution of $A_{THz}(\Omega,z)$ is given below in (4-2).

$$\begin{aligned}\frac{dA_{THz}(\Omega,z)}{dz}&=-\frac{\alpha(\Omega)}{2}A_{THz}(\Omega,z)\\&-\frac{j\Omega^2}{2c^2k(\Omega)}\chi_{eff}^{(2)}(z)\int_0^\infty A_{op}(\omega+\Omega,z)A_{op}^*(\omega,z)e^{-j[k(\omega+\Omega)-k(\omega)-k(\Omega)]z}d\omega\end{aligned} \tag{4-2}$$

Here, the first term on the right hand side (RHS) corresponds to the THz loss due to absorption, which may include background as well as FCA. The second term corresponds to the second order non-linear polarization due to OR. Noticing this term, it is clear that OR is nothing but an aggregate of all possible difference frequency generation (DFG) processes within the bandwidth of the optical pulse. It can be seen that setting the exponential factor inside the integral on the RHS of (4-2) to zero, gives the well-

known phase matching condition $n(\Omega)\cos\gamma = n_g(\omega_0)$ for OR using tilted-pulse-fronts. In (4-2), the parameter $\chi_{eff}^{(2)}(z) = 2d_{eff}(z)$ is the effective second order non-linear susceptibility at the spatial co-ordinate z. For the calculations in this chapter, $\chi_{eff}^{(2)}(z)$ is constant in space. However, by introducing spatial variations in $\chi_{eff}^{(2)}(z)$, the model can also be used to analyze quasi-phase-matching (QPM) structures. Thus, the developed model can be used to simulate a number of devices based on OR. If only (4-1)-(4-2) are solved, we would be working in the undepleted pump approximation.

In order to account for pump depletion and spectral re-shaping of the optical pump, we write the corresponding equations for the evolution of $A_{op}(\omega, z)$ in (4-3). Equations (4-1)- (4-3) conserve energy in the absence of any dissipative processes, which indicate that the theory is on solid ground. A proof of this is provided in Appendix B.

$$\begin{aligned}
&\frac{dA_{op}(\omega,z)}{dz} = \frac{-\alpha_{op}A_{op}(\omega,z)}{2} \\
&-\frac{j\omega^2}{2c^2k(\omega)}\chi_{eff}^{(2)}(z)\int_0^\infty A_{op}(\omega+\Omega,z)A_{THz}^*(\Omega,z)e^{-j[k(\omega+\Omega)-k(\omega)-k(\Omega)]z}d\Omega \\
&-\frac{j\omega^2}{2c^2k(\omega)}\chi_{eff}^{(2)}(z)\int_0^\infty A_{op}(\omega-\Omega,z)A_{THz}(\Omega,z)^{-j[k(\omega-\Omega)-k(\omega)+k(\Omega)]z}d\Omega \\
&+\mathbf{F}\left\{j\frac{\varepsilon_0\omega_0 n(\omega_0)^2 n_2(z)}{2}\left|A_{op}(z,t)\right|^2 A_{op}(z,t)\right\}+\mathbf{F}\left\{j\frac{\varepsilon_0\omega_0 n(\omega_0)^2 n_2(z)}{2}\left[\left|A_{op}(z,t-t')\right|^2\otimes h_r(t')\right]A_{op}(z,t)\right\}
\end{aligned} \tag{4-3}$$

In (4-3), the first term corresponds to the absorption of the optical radiation. The second term is analogous to the second term in (4-2), and represents the cascaded down-conversion of the optical frequency due to THz generation. The third term represents the up-conversion of optical frequency components due to sum frequency generation (SFG) between an optical frequency component at $(\omega-\Omega)$ and a THz field component at Ω. The fourth term corresponds to SPM. Here ε_0 is the permittivity of free space and $n_2(z)$ is the non-linear refractive index coefficient at spatial co-ordinate z. The symbol **F** is used to denote the temporal Fourier transform. It can be seen that the effects of SPM are directly proportional to the optical field intensity. The final term corresponds to SRS. Here $h_R(\omega')$ represents the Raman gain spectrum. The complex second order nonlinear polarization terms on the right hand side of (4-2)-(4-3), were calculated rapidly by expressing them in terms of Fourier transforms. A 4th order Runge-Kutta (See Appendix C) method was used to numerically solve the above equations with a spatial resolution of 10 μm. This spatial resolution was verified to achieve numerical convergence (See Appendix C).

4.2 Validation of model: Comparison to experimentally measured optical spectra

In order to validate the developed 1-D model, we simulate the transmitted spectrum of the optical pump pulse at various levels of THz generation for the experimental parameters presented in [14]. The optical pump pulse used in [14] was modeled by a transform limited 500 fs Gaussian pulse centered at 1031.8 nm with a maximum fluence of 20 mJ/cm^2. The second order effective non-linear susceptibility $\chi_{eff}^{(2)} = 2d_{eff}$

was assumed to be 360 pm/V [30]. A non-linear refractive index value of $n_2 = 10^{-15}$ cm^2/W [31] was used to account for SPM and SRS effects. The Raman gain spectrum was obtained from measurements in [32] The refractive index and absorption coefficient data at optical and THz frequencies were obtained from [33]. At 1 μm pump wavelengths, FCA of THz radiation occurs mainly due to free-carriers generated by four-photon absorption of the optical radiation. Experimental fits [34] have estimated a four-photon absorption coefficient of 10^{-7}cm^5/GW^3 and a THz FCA cross section of 2×10^{-21} cm^2. Corresponding to these values, even a 500fs pulse with peak intensity of 150 GW/cm^2 will result in a FCA coefficient of only ~0.1cm^{-1} , which is much smaller than the background absorption coefficient of lithium niobate (~10cm^{-1} at room temperature [33]). Therefore, for the peak intensities of 40 GW/cm^2 used in the simulations below, FCA and four-photon absorption coefficients can be effectively set to zero with negligible loss in accuracy. The crystal temperature was assumed to be 290K. The pulse-front-tilt angle for optimal phase matching at 290K was $\gamma = 63.09^\circ$. A Fresnel reflection loss of ~44% due to the high refractive index of lithium niobate at THz frequencies is included in the calculations.

In the actual physical situation, different parts of the optical pump beam see different propagation lengths due to the prism geometry of the crystal in OR using tilted-pulse-fronts. This situation can be modeled accurately only with a 2-D spatial model, as will be done in Chapter 5. However, in the 1-D model, an effective propagation length L_{eff} is used. The simulated spectra of the transmitted optical pulses are plotted in Fig.4-1 along with the experimental results. The conversion efficiency is tuned by changing the pump fluence from zero to a maximum of 20 mJ/cm^2. This mimics the rotation of polarization in the actual experiment. The maximum conversion efficiency at room temperature was reported to be 1.15% in [14]. We obtain a maximum value of 0.8% in our simulations, which is in good agreement with the experimental results. The difference in results can be attributed to small uncertainties in material parameters ($\chi^{(2)}_{eff}, n_2, \alpha_{THz}$) and experiments. In particular, there is uncertainty in the absorption coefficients below 0.9 THz [33].

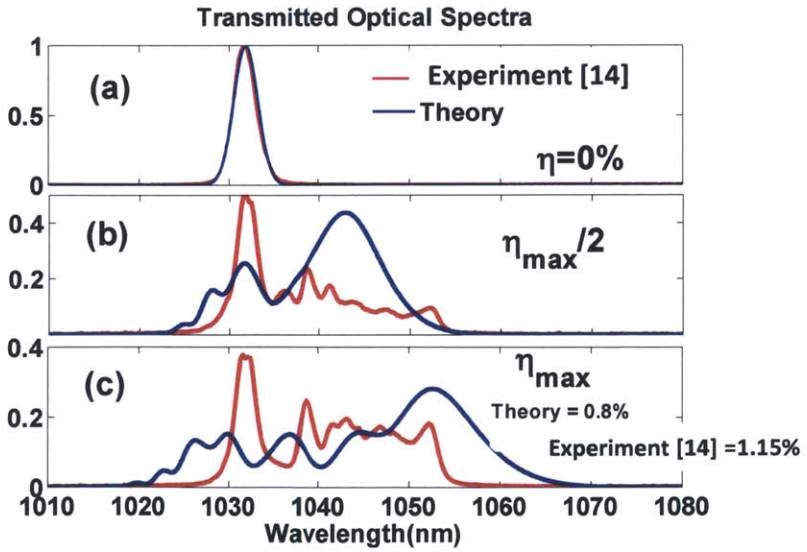

Figure 4-1 : Comparison of experimental and simulated optical spectra for different amounts of generated THz. The frequency down-shift and spectral broadening can be modeled only by the simultaneous solution of the THz and optical fields. (a) No broadening or red-shift is observed when conversion efficiency $\eta = 0$ % , which implies small

effect of SPM. (b)There is large cascaded frequency down-shift and spectral broadening corresponding to a larger amount of THz generation (c) Maximum frequency down-shift and spectral broadening is observed when conversion efficiency is maximum at η_{max}=0.8%. Conversion efficiency, amount of frequency down-shift and spectral broadening are in good agreement with experiments [14]. The difference between theory and experiment can be attributed to uncertainties in material parameters ($\chi_{eff}^{(2)}, n_2, \alpha_{THz}$) and experiments. The measured spectra include spatial averaging effects which are not included in the calculations, which could explain their difference.

In Figs. 4-1(a)-4-1(c), both the simulated and experimental spectra show an amount of broadening and red-shift commensurate with the amount of THz generated. This is strong evidence that the observed broadening is a direct consequence of THz generation. To further reinforce this point, in Fig. 4-1(a), when there is virtually no THz generation, there is also negligible broadening of the transmitted optical pump pulse. This also indicates a relatively small impact of SPM and SRS effects in these experiments even at the relatively large peak intensities of 40 GW/cm^2.

In Figs. 4-1(b) and 4-1(c), the extent of broadening seen in experiments is well reproduced by the simulations at half the maximum and maximum conversion efficiency, respectively. Here, in addition to the red shift, a relatively small amount of blue-shift is also seen which also increases with increasing THz generation. This effect is also observed in our calculations. An explanation for this is obtained by inspecting the third term on the right hand side of (4-3). This term represents a blue-shift of the optical pulse via THz plus optical SFG, which increases with the THz conversion. Consequently, there is an increasing amount of blue-shift with increased THz generation, albeit to a much lesser extent than that of the red-shift. The difference in the shape of the spectra between experiments and simulations is partly due to the usage of a 1-D model. In the actual physical situation, due to the non-collinear propagation of the optical and THz radiation, different parts of the optical beam will be broadened to different extents. The final recorded power spectrum would then correspond to a spatial averaging of the spectral intensity over the beam cross-section. Such spatial averaging has not been considered here.

The good match in conversion efficiency, frequency shifting, and spectral broadening between simulation and experiments is evidence that even this simple 1-D model captures the essential physics of the nonlinear THz generation process.

4.3 Limitation of conversion efficiency due to cascading effects

In 4.2, we established the accuracy of our model by obtaining good quantitative agreement with experiments in conversion efficiency values and transmitted optical spectra. We now use the model to show that cascading effects in conjunction with GVD-AD represent the strongest limitation to THz generation for 1μm pumping. We selectively switch-on and switch-off, various effects in our simulations to study their relative importance.

In Fig. 4-2, we calculate the conversion efficiency as a function of the effective propagation length- L_{eff} for various cases. Material dispersion and THz absorption are considered in all cases. The different cases are as follows :- (i) GVD-AD is considered. This corresponds to an undepleted pump approximation where only Eqs. (4-1),(4-2) are used. There is no change in the total pump pulse energy or spectrum; (ii) SPM, SRS and GVD-AD are considered. Equations (4-1) and (4-2) are used. Only the fourth and fifth terms in (4-3) are employed. Here, the total pump pulse energy is conserved but spectral re-shaping of the pump pulse spectrum occurs due to SPM; (iii) cascading effects are included but SPM, SRS and GVD-AD are excluded. Equations (4-1a), (4-2) and the first three terms of (4-3) are utilized. The second term of (4-1a) $k''(\omega)_{AD}$ is set to zero; (iv) cascading effects and GVD-AD are included but SPM and SRS are

excluded. Equations (4-1)- (4-3) are used but the fourth and fifth terms of (4-3) are ignored;(v) all effects are simultaneously included (Eqs.(4-1)-(4-3)). A crystal temperature of 100K is assumed. This is because the difference between various cases is best illustrated with cryogenic cooling rather than at room temperature. The pump fluence is fixed at 20 mJ/cm^2 for all simulations as in Section 4.2. The material parameters are the same as in Section 4.2, except for absorption and refractive index which are functions of crystal temperature. Due to the change in refractive index with temperature, the pulse-front-tilt angle for optimal phase matching is now set to $\gamma = 62.26^{\circ}$.

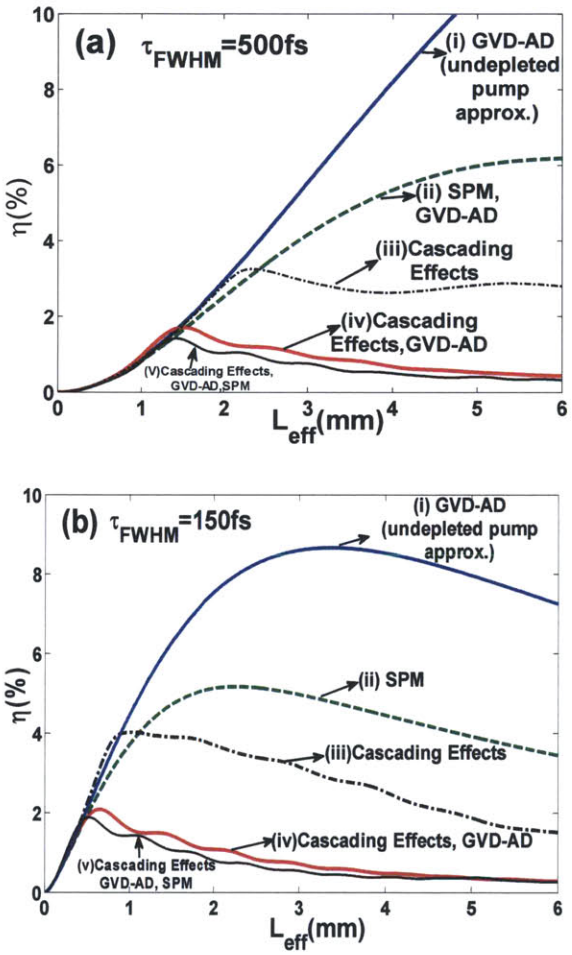

Figure 4-2: Conversion efficiencies as a function of effective length are calculated by switching on and switching off various effects. Material dispersion and absorption are considered for all cases. The pump fluence is 20 mJ/cm^2, $\chi_{eff}^{(2)} = 360 pm/V$, n_2=10^{-15} cm^2/W and crystal temperature is 100K.(a) Gaussian pulses with 500 fs pulse width at FWHM with peak intensity of 40 GW/cm^2 are used. Cascading effects together with GVD-AD leads to the lowest conversion efficiencies. The drop in conversion efficiency is attributed to the enhancement of phase mismatch caused by dispersion due to the large spectral broadening caused by THz generation (See Figs. 4-1(b)-(c)). However, since group velocity dispersion due to angular dispersion (GVD-AD) is more significant than group velocity dispersion due to material dispersion at optical frequencies in lithium niobate, cascading effects in conjunction with GVD-AD is the strongest limitation to THz generation. SPM effects are much less detrimental since they cause relatively small broadening of the optical pump spectrum (see Fig. 4-1(a)). (b) Cascading effects along with GVD-AD are most detrimental even for a 150 fs Gaussian pulse with three times larger peak intensity.

In Fig. 4-2 (a), we plot the simulation results for cases (i)-(v) for a transform limited Gaussian pulse with a pulse width of 500 fs at FWHM. This corresponds to a peak intensity of 40 GW/cm^2. For case (i), when only GVD-AD is considered, conversion efficiencies larger than 10% are possible, in agreement with the results from [16]. For case (ii), when SPM and SRS effects are included, the conversion efficiency peaks at about 6%. The reduction in maximum conversion efficiency is because of the additional phase mismatch induced by the change in refractive index at optical frequencies due to SPM effects. The increase in phase mismatch is evident in the reduction of the optimal effective length value compared to case (i) to L_{eff} = 6 mm. Beyond this distance, the coherent build up of THz energy reduces as the optical and THz pulses slip out of phase.

In case (iii), when only cascading effects are considered along with material dispersion, the conversion efficiency peaks at ~3%. Here, the dispersive effects due to material dispersion are enhanced by the broadened spectral bandwidth of the optical pump pulse and therefore the corresponding optimal effective lengths are shorter compared to cases (i),(ii).This is demonstrated by a decrease of the optimal effective length to ~2.5 mm. This shows that cascading effects in combination with material dispersion are even more detrimental to THz generation than SPM. This trend agrees with the experiments and simulations in Fig. 4-1. Here, it was seen that the spectral broadening which occurs as a consequence of THz generation was much larger than that due to SPM.

In case (iv), when both cascading effects and GVD-AD are considered, the peak conversion efficiency is reduced to 1.8%. The optimal effective length reduces even further compared to case (iii) to ~1.5 mm. It can also be seen that the conversion efficiency degrades more rapidly with propagation length compared to case (iii). These allude to the dominant effect of GVD-AD compared to material dispersion. This is further verified by calculations of GVD-AD from (4-1b) (-15000 fs^2/mm) which are significantly larger in magnitude compared to group velocity dispersion due to material dispersion in lithium niobate at optical frequencies (<1000 fs^2/mm). Finally, if all effects (SPM, GVD-AD, cascading effects) are considered simultaneously in case (v), there is only a minor change compared to case (iv) in Fig. 4-2(a). This confirms that the combination of spectral broadening caused by the generation of THz (cascading effects) and angular dispersion are the most dominant limiting effects. A five-fold reduction in the maximum achievable conversion efficiency in comparison to the 10% efficiency levels for similar pump parameters [10] is observed.

In Fig. 4-2(b), we show the results for cases (i)-(v), using a transform limited Gaussian pulse with a pulsewidth of 150 fs at FWHM, while keeping the pump fluence constant. This corresponds to a peak intensity of ~120 GW/cm^2. At these higher intensities, the effect of SPM is seen to be more pronounced than in Fig. 4-2(a). However, even here trends are consistent with Fig. 4-2(a) and cascading effects in conjunction with GVD-AD impose the strongest limitation to conversion efficiency. The effective length at which conversion efficiency peaks reduces even further compared to Fig. 4-2(a) for all cases. In case (i), this is because of the larger effects of dispersion due to an increased spectral bandwidth compared to Fig. 4-2(a). In cases (ii)-(iv), it is owed to a faster (with respect to length) broadening of the optical pump pulse. This is because THz generation initially occurs at a faster rate because of the higher intensity. However, since the generation of THz is necessarily accompanied by spectral broadening of the optical pump pulse, coherent build-up of THz ceases at shorter distances.

4.4 A time-domain description

The rapid degradation of conversion efficiency with L_{eff} can be understood more intuitively from a time domain view point. In Fig. 4-3 (a)-(f), we present snapshots of the spatial intensity profiles of the optical pump pulse at various times. The simulation parameters are the same as those used for Fig.4-2(a). In Figs. 4-3(a)-(c), only SPM and GVD-AD effects are considered. As the optical pulse propagates through the nonlinear material, it is spectrally broadened due to SPM. Due to increasing spectral bandwidth with propagation distance, the effects of dispersion become more adverse and the peak intensity of the pulse drops as it broadens in time. The drop in peak intensity is accompanied with a drop in conversion efficiency as expected. Comparing Fig. 4-3(a) to 4-3(c), the peak intensity drops by about 2.5 times over the entire propagation distance. This effect is much more drastic when cascading effects and GVD-AD are considered as seen in Figs. 4-3 (d)-(f). Here, the pulse shape is severely broadened and distorted in time due to the much larger spectral broadening in comparison to SPM. The drop in peak intensity from Fig.4-3 (d) to Fig. 4-3(f) is about 7 times. In addition, there is a severe break-up of the pulse in time. This means different parts of the pump are generating THz radiation incoherently, which prevents further coherent build-up of THz radiation. Therefore, the rapid degradation of conversion efficiency when cascading effects and GVD-AD are considered can also be viewed as a consequence of the drop in peak intensity and spatio-temporal break-up of the pulse.

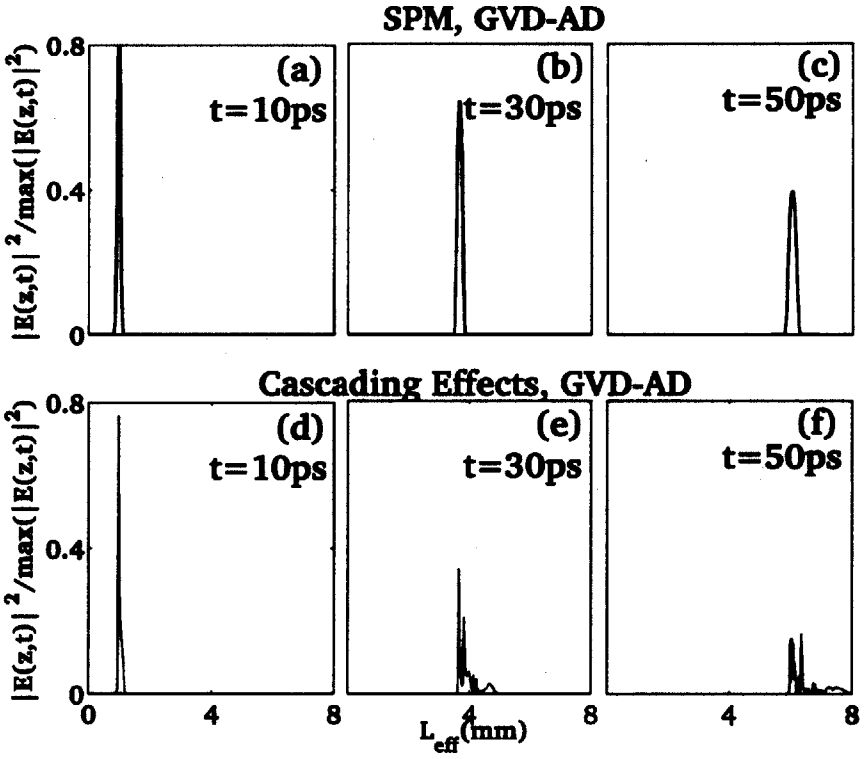

Figure 4-3: Snapshots of spatial profiles of optical pump pulse at various times. (a)-(c) include only SPM effects and dispersion (GVD-AD and material dispersion). Dispersion spreads the pulse in time, reducing intensity which leads to saturation of conversion efficiency. (d)-(f) include only cascading effects and dispersion. The pulse is dispersed much more rapidly compared to (a)-(c) due to the large spectral broadening.

4.5 Limitations to optical rectification for 800nm pumping

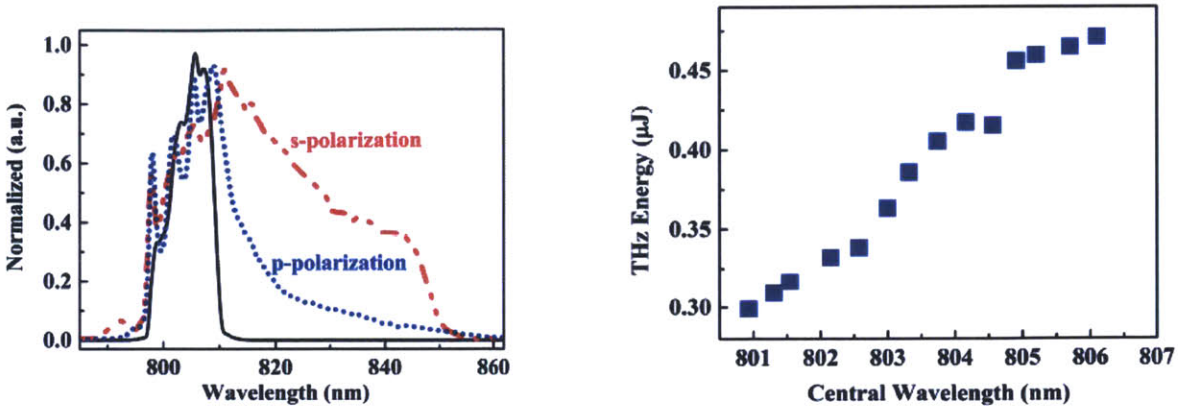

Figure 4-4. (a) Experimental curves [29] indicating the relative broadening due to SPM and cascading effects for pumping by 150fs Ti: Sapphire lasers centered at 800 nm wavelength. Even for these shorter wavelengths/pulse durations, cascading effects dominate SPM due to the larger extent of broadening. (b) In addition to cascading effects, three-photon absorption also plays a critical role in impeding THz generation. As the intensity gets higher, three-photon absorption of the optical pump increases leading to a larger amount of free-carrier absorption of THz radiation.

In this section, we provide a brief summary of experimental results [29] which followed up on our earlier theoretical predictions [22] to confirm that cascading effects in conjunction with dispersive effects is the strongest limitation to THz generation by optical rectification using tilted-pulse-fronts, even for pumping by 800 nm pulses. In Fig.4-3(a), we present the results of spectral broadening with and without THz generation, which confirms that spectral broadening in the absence of THz generation is significantly smaller. This alludes once again to a smaller impact of SPM even for systems pumped by 150fs 800nm pulses.

Fig. 4-3(b) shows the emitted THz energy as function of the central wavelength (λ_c) of the pump pulses for a fixed pulse duration τ=298 fs and pump fluence of 7.6 mJ/cm^2.The generated THz energy monotonically increased with the central wavelength of the pump laser. When the central wavelength increased from 801 nm to 806 nm, the THz energy was enhanced by ~50%. This observation indicates that the central wavelength of the pump laser has a strong influence on the THz generation in this frequency range. We associate this dependence with 3PA. In fact, the direct band gap (E_g) of lithium niobate is in the range of 4 eV at room temperature and a significant nonlinear absorption rate may originate from 3-photon interband transitions, where the photon energy ($\hbar\omega$) is~1.55 eV, even at moderate intensities of up to a few tens of GW/cm^2. For a given radiation intensity, the interband 3PA scales approximately linearly with photon energy in the case $3\hbar\omega > E_g$ [35], which is the case for 3PA in lithium niobate with a radiation wavelength centered around 800 nm. This process limits the conversion efficiency by significantly increasing the free carrier density, which then strongly absorbs THz radiation. In previous work [16], FCA was cited as an important factor for saturation of THz energy. However, in [18] it was suggested that FCA plays no significant role in the OR processes in lithium niobate and has no effect at all in THz energy saturation. Moreover, SPM was recognized to be the only factor in the saturation of THz energy. The results shown in Fig. 4-3(b) depict for the first time a strong correlation between pump photon energy distribution on generated THz radiation and is evidence of the role played by FCA arising from 3PA.

In summary, cascading effects broaden the spectral bandwidth which enhances dispersive effects and compromises phase-matching. In lithium niobate, since GVD-AD due to angular dispersion is larger than

that due to material dispersion at optical frequencies, cascading effects in conjunction with GVD-AD represent the strongest limitation to THz generation for 1 μm pumping. The inclusion of these effects significantly reduces the maximum achievable conversion efficiency. The effective lengths at which the conversion efficiency peaks reduce significantly and are on the order of ~1 mm. For such short propagation lengths, absorption plays a minor role in limiting conversion efficiency. This is an additional reason why FCA is not expected to play a major role for pumping at 1 μm. For 800 nm pumping, in addition to cascading effects and GVD-AD, three-photon absorption may lead to considerable FCA of THz radiation [29].

5. The 2-D depleted model

In Chapter 2, we provided an overview of the physics at work in optical rectification. In Chapters 3-4, we built up the complexity of the theory to a point that we now can dive into a comprehensive two dimensional model which simultaneously accounts for (i) spatio-temporal distortions of the optical pump pulse, (ii) cascading effects, (iii) SPM and SRS effects, (iv) material dispersion and absorption as well as (v) nonlinear crystal geometry. An outline of the approach is as follows. The spatio-temporal distortions imparted to the optical pump pulse by arbitrary imaging systems are modeled analytically via dispersive ray pulse matrices. The emergent electric field of the optical pump pulse from the imaging system is used as an initial condition to solve for THz and optical fields via a system of coupled nonlinear 2-D wave equations. Spatial Fourier decomposition and appropriate co-ordinate transformations enable an efficient solution of this coupled system of nonlinear equations. The use of spatial Fourier decomposition also enables reflections of the THz radiation at the crystal boundary and subsequent propagation to be modeled with relative ease. The developed model is applicable to the simulation of a variety of OR systems with different imaging systems, crystal geometries and optical pump pulse formats.

We validate the model by comparisons of the optimal imaging configuration to analytic calculations, which show good agreement. The impact of imaging errors on conversion efficiency is shown quantitatively. It is seen that small perturbations to the optimal imaging configuration can result in sizeable degradation of conversion efficiency and modification of THz radiation properties. We discuss the meaning of effective interaction length in a 2-D geometry. It is seen that conversion efficiency drops with beam size, which is a concern for scaling THz energies to the 10 mJ level by increasing the optical pump pulse energy. We illustrate how the optimization of conversion efficiency in such setups is highly dependent on the properties of the pump pulse. Furthermore, the optimization of conversion efficiency is seen to negatively impact other properties such as the THz beam quality. This suggests that multiple factors must be considered while designing such systems.

5.1 Theory

5.1.1 Propagation of optical pump fields through the optical setup

All THz generation systems based on nonlinear optical processes include some form of imaging optics. The imaging system transforms the beam size and radius of curvature of the optical pump. The variation of beam size changes the localized intensity whereas the finite beam size and curvature affect phase matching by introducing a finite momentum (k_x) distribution. Thus, output parameters such as conversion efficiency, THz spectrum and THz beam propagation are linked to the imaging system configuration. In non-collinear phase matching geometries, the role of the imaging system is even more critical. For instance, for OR using tilted-pulse-fronts, imaging errors due to incorrect magnification or grating angle affects phase matching by altering the pulse-front-tilt angle. Thus, a means to provide a correlation between the THz spectrum, THz beam propagation and conversion efficiency to the imaging system configuration would be very useful to quantify imaging errors and locate optimal imaging conditions for a variety of different imaging systems.

In this section, we show how to account for the effects of the imaging system by employing dispersive ray pulse matrices. This approach enables us to determine the modification of the optical pump field by an

arbitrary set of optical components. Since, the beam size of the optical pump is typically much larger than the optical wavelength, paraxial approximations of ray-pulse matrix schemes are valid. Each spectral component $E_{op}^{in}(\omega, x_o, z_o)$ of the optical pump pulse at angular frequency ω, with input beam centred at a transverse position $x_{in}(\omega)$ and propagation direction $x_{in}^{'}(\omega)$ emerges with transverse position $x_{out}(\omega)$ and propagation direction $x_{out}^{'}(\omega)$ from the optical setup, just before entering the nonlinear crystal.

The dependence of position and propagation direction on frequency accounts for spatial chirp and angular dispersion. The propagation direction here is not the physical direction but one normalized by the refractive index of the medium [24], which makes it convenient to apply to systems with interfaces of mismatched refractive index. The relationship between $x_{in}(\omega)$, $x_{in}^{'}(\omega)$ and $x_{out}(\omega)$, $x_{out}^{'}(\omega)$ is given by (5-1a). In (5-1a), $\overline{\overline{M(\omega)}}$ is the overall ray pulse matrix of the imaging system and is given by the product of the ray pulse matrices of individual optical components $\overline{\overline{M_i(\omega)}}$ in reverse order of incidence as shown in (5-1b). Here, propagation in free space is also considered to be an 'optical component'. The beam positions and propagation directions after the i^{th} optical element, $x_{out_i}(\omega)$ and $x_{out_i}^{'}(\omega)$ can be obtained using (5-1c). Note that the matrices are functions of frequency to incorporate dispersion.

$$\overline{\overline{M(\omega)}}\begin{bmatrix} x_{in}(\omega) \\ x_{in}^{'}(\omega) \\ 1 \end{bmatrix} = \begin{bmatrix} x_{out}(\omega,0) \\ x_{out}^{'}(\omega,0) \\ 1 \end{bmatrix} \tag{5-1a}$$

$$\overline{\overline{M(\omega)}} = \overline{\overline{M_n(\omega)}}..\overline{\overline{M_i(\omega)}}..\overline{\overline{M_1(\omega)}} \tag{5-1b}$$

$$\overline{\overline{M_i(\omega)}}...\overline{\overline{M_2(\omega)M_1(\omega)}}\begin{bmatrix} x_{in}(\omega) \\ x_{in}^{'}(\omega) \\ 1 \end{bmatrix} = \begin{bmatrix} x_{out_i}(\omega) \\ x_{out_i}^{'}(\omega) \\ 1 \end{bmatrix} \tag{5-1c}$$

The ray pulse matrix of the i^{th} optical component $\overline{\overline{M_i(\omega)}}$ can be described by a 3x3 matrix for a single transverse spatial dimension as shown in (5-2). If instead, we consider both transverse spatial dimensions, then we would have a 6x6 matrix instead.

$$\overline{\overline{M_i(\omega)}} = \begin{bmatrix} \left.\frac{\partial x_{out_j}}{\partial x_{in}}\right|_i & \left.\frac{\partial x_{out}}{\partial x_{in}^{'}}\right|_i & \left.\frac{\partial x_{out}}{\partial \omega}\right|_i (\omega-\omega_0) \\ \left.\frac{\partial x_{out}^{'}}{\partial x_{in}}\right|_i & \left.\frac{\partial x_{out_j}^{'}}{\partial x_{in}^{'}}\right|_i & \left.\frac{\partial x_{out}^{'}}{\partial \omega}\right|_i (\omega-\omega_0) \\ 0 & 0 & 1 \end{bmatrix} = \begin{bmatrix} A_i(\omega) & B_i(\omega) & E_i(\omega) \\ C_i(\omega) & D_i(\omega) & F_i(\omega) \\ 0 & 0 & 1 \end{bmatrix} \tag{5-2}$$

Equation (5-2) shows that the upper 2x2 matrix is nothing but the standard ABCD matrix for Gaussian beams. However, in order to account for dispersion, there are two additional terms E_i and F_i which correspond to the partial derivatives $\partial x_{out}/\partial\omega|_i$ and $\partial x'_{out}/\partial\omega\Big|_i$. These terms refer to the shift in output beam position and output beam propagation direction in response to a shift in frequency. The subscripts *i* indicate that they are different for various optical components. Typically, the $E_i(\omega)$ and $F_i(\omega)$ terms are calculated upto the second order in $(\omega-\omega_0)$, which leads to an overall third order dependence on frequency of terms. We provide expressions with up to a fourth order dependence on frequency for common optical components in Appendix C. Note that the last row of $\overline{\overline{M_i}}(\omega)$ is [0 0 1] for passive optical elements as the source frequency does not change.

With the knowledge of the input and output beam positions and propagation directions, a Huygen's integral can be used as shown in [36] to calculate the electric field of the optical pump after it has passed through the imaging system. In this paper, a paraxial Gaussian beam is assumed for which the expression for the electric field reduces to (5-3).

$$E_{op}^{out}(\omega,x_0,z_0)=\sqrt{\frac{\sigma_{in}(\omega)}{\sigma_{out}(\omega,z_0)}}\cdot E_0 e^{-jk\frac{(x_0-x_{out}(\omega,z_0))^2}{2q_{out}(\omega,z_0)}} e^{-jkx'_{out}(\omega,z_0).x_0} e^{-j[\phi_0(\omega,z_0)+\phi_1(\omega,z_0)+\phi_2(\omega,z_0)+\phi_3(\omega,z_0)]} \tag{5-3a}$$

$$\phi_0(\omega)=k\sum_{i=1}^{N}L_i n_i(\omega) \tag{5-3b}$$

$$\sqrt{\frac{1}{A(\omega,z_0)+B(\omega,z_0)/q(\omega)_{in}}}=\sqrt{\frac{\sigma_{in}(\omega)}{\sigma_{out}(\omega,z_0)}}e^{-j\varphi_1(\omega,z_0)} \tag{5-3c}$$

$$\phi_2(\omega,z_0)=\frac{k}{2}[x_{in}(\omega)x'_{in}(\omega,z_0)-x_{out}(\omega)x'_{out}(\omega,z_0)] \tag{5-3d}$$

$$\phi_3(\omega,z_0)=\frac{k}{2}\sum_{i=1}^{N}F_i(\omega)x_{out_{i+1}}(\omega) \tag{5-3e}$$

In (5-3a), $\sigma_{in}(\omega),\sigma_{out}(\omega)$ are the beam radii of the spectral component at ω at the input and output of the imaging system respectively. The pre-factor $\sqrt{\sigma_{in}(\omega)/\sigma_{out}(\omega)}$ in (5-3a) represents the change in the optical field intensity as a consequence of energy conservation. The second term in (5-3a), represents the transverse variation of the beam along the x_0 co-ordinate axis, where q_{out} is the output q parameter associated with Gaussian beams and is calculated with the usual A,B,C,D terms of the overall matrix $\overline{\overline{M}}$. Notice that each spectral component is centered at a different beam position $x_{out}(\omega,z_0)$, which accounts for spatial-chirp. Furthermore, this beam position is a function of space, i.e it changes as the optical pulse propagates. The finite beam size in the transverse (x_0) dimension results in a finite momentum (k_x) distribution, which in turn affects phase matching. The third term, $e^{-jkx'_{out}(\omega,z_0).x_0}$ represents angular dispersion which also directly influences phase matching. Since, the value of x'_{out} is mapped to the

configuration of the imaging system (grating angle, imaging distances etc), (5-3a) abets in quantifying the impact of imaging errors on the properties of THz radiation (spectrum, propagation, conversion efficiency). The various phase terms in (5-3a), $\phi_0(\omega),\phi_1(\omega),\phi_2(\omega),\phi_3(\omega)$ are given by (5-3b)-(5-3e). The $\phi_0(\omega)$ term represents the overall phase delay due to propagation through the setup where L_i represent propagation distances through various optical components and $n_i(\omega)$ are the corresponding refractive indices of each optical component at various optical frequencies. The $\phi_1(\omega)$ term represents the correction to $\phi_0(\omega)$ due to a Gaussian beam. The remaining terms $\phi_2(\omega)$ and $\phi_3(\omega)$ account for all other dispersion other than material dispersion and include the higher order phase terms. Thus using the ray pulse matrices, one obtains an explicit expression for the electric $E_{op}^{out}(\omega,x_0,z_0)$ field for every spectral component of the optical pump pulse spectrum. This calculated $E_{op}^{out}(\omega,x_0,z_0)$ value will be used as an initial condition to solve the nonlinear coupled system of wave equations. This expression accounts for spatial variations angular dispersion, spatial frequency-variations and spatial variations in pulsewidth. Thus a one-to-one correspondence between the imaging system configuration and the properties of THz radiation can be established.

5.1.2 Nonlinear polarization due to optical rectification

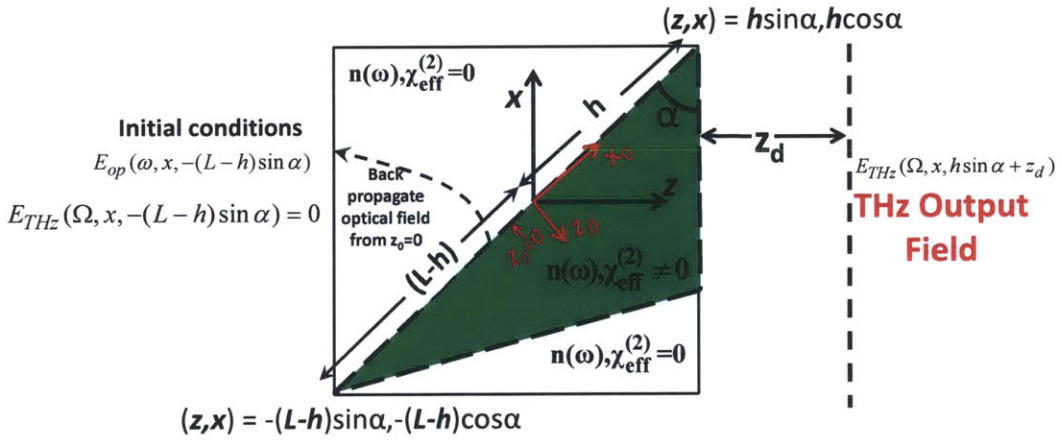

Figure 5-1: 2-D computational space for solving coupled nonlinear wave equations for optical rectification. Nonlinear crystal geometry is accounted for by delineating an appropriate distribution of $\chi^{(2)}(x,z)$. Edges of the distribution are smoothed out to avoid discontinuities. The refractive index is homogeneously distributed throughout the computational space. The optical beam is centered at a distance h from the apex of the crystal which sets the limits to the computational region. The optical field at the beginning of the lattice is calculated analytically using dispersive ray pulse matrices.

In Section 5.1.1, we obtained the electric field of the optical pump pulse inside the crystal in the co-ordinate system (x_0, z_0) as shown in Fig.5-1. In this section, we show how to calculate the nonlinear polarization terms which drive the optical and THz fields. The nonlinear crystal has an apex angle γ, where γ is designed to be approximately equal to the pulse-front-tilt angle of the optical pump pulse. This design ensures that the generated THz radiation emerges approximately normal to the air-crystal interface for maximum THz extraction. In order to treat crystal geometry and reflection at the crystal boundary efficiently, it is prudent to work in transformed co-ordinates (x, z) where z is now along the direction of the normal to the air-crystal interface and x is the corresponding transverse direction as shown in Fig.5-1

The origin of the (x,z) co-ordinate system is taken to be the central position of the input optical pump pulse and is located at a distance h from the crystal apex along the input crystal face of length L as shown in Fig.5-1. Since all the THz radiation, emerges about a relatively small cone around the normal or equivalently with a small spread in transverse momentum k_x, the requirements for spatial resolution Δx for Fourier decomposition in the (x,z) co-ordinate system are much coarser compared to the case of working in the (x_0,z_0) co-ordinate system. Thus in addition to mathematical convenience, the co-ordinate transformation also alleviates computational cost. The transformation rules from (x, z) to (x_0,z_0) are obtained straightforwardly via projection and are presented in (5-4).

$$x_0 = x\cos\gamma + z\sin\gamma \tag{5-4a}$$

$$z_0 = -x\sin\gamma + z\cos\gamma \tag{5-4b}$$

The electric field $E_{op}^{out}(\omega,x_0,z_0)$ obtained from (5-3) is used as an initial condition to solving the nonlinear system of coupled wave equations. We can use (5-4) in (5-3), to obtain the electric field of the optical pump pulse in the transformed co-ordinates i.e. $E_{op}^{out}(\omega,x,z)$. The value of $E_{op}^{out}(\omega,x,z)$ at $z=-(L-h)\sin\alpha$ serves as the initial condition for the evolution of wave equations described in Section 5.1.3. We first present the various nonlinear polarization terms which drive the wave equations in Section 5.1.3.

Equation (5-5) describes the nonlinear polarization term $P_{THz}(\Omega,x,z)$ due to optical rectification (OR) which drives the THz electric field $E(\Omega,x,z)$ at the angular frequency Ω.

$$P_{THz}(\Omega,x,z) = \varepsilon_0\chi_{eff}^{(2)}(x,z).\int_0^{\infty} E_{op}(\omega+\Omega,x,z)E_{op}{}^*(\omega,x,z)d\omega \tag{5-5}$$

In (5-5), $E_{op}(\omega+\Omega,x,z)$ corresponds to the electric field of the spectral component of the optical pump pulse spectrum at angular frequency ω and spatial location (x,z). The nonlinear polarization term at each spatial location (x,z) in (5-5) can be seen to be an aggregate of all possible DFG processes between the spectral component $E_{op}(\omega+\Omega,x,z)$ and $E_{op}(\omega,x,z)$. If one substitutes the expression for the electric field from (5-3a). In (5-5), various effects which affect phase matching effects become evident. For instance, because of the angular dispersion term in (5-3a), a term proportional to $e^{-j\left[\left(\frac{\omega+\Omega}{c}x_c'(\omega+\Omega,x,z)-\frac{\omega}{c}x_c'(\omega,x,z)\right)x+\varphi_0(\omega+\Omega)-\varphi_0(\omega)\right]}$ appears in (5-5) which enables us to quantify the effect of phase-mismatch due to imaging errors. Similarly, a term proportional to $e^{-j\left[\frac{\omega+\Omega}{c}\frac{(x_0-x_{out}(\omega+\Omega))^2}{2q_{out}(\omega+\Omega)}-\frac{\omega}{c}\frac{(x_0-x_{out}(\omega))^2}{2q_{out}(\omega)}\right]}$ describes a spatial variation in the magnitude of $P_{THz}(\Omega,x,z)$ leading to spatial variation of the generated THz frequency. This term also describes the effects of the finite radius of curvature of the optical pump pulse. In addition, substituting (5-3a) in (5-5) produces terms of the form $e^{-j[\phi_1(\omega+\Omega)-\phi_1(\omega)+\phi_2(\omega+\Omega)-\phi_2(\omega)+\phi_3(\omega+\Omega)-\phi_3(\omega)]}$ which gives the effect of phase mismatch due to various phase

accumulations through the optical setup. In (5-5), $\chi_{eff}^{(2)}(x,z)$ is the effective second order nonlinear susceptibility for OR at each spatial location and ε_0 is the free space permittivity. The spatial dependence of the effective non-linear susceptibility is used to account for the geometry of the non-linear crystal as shown in Fig.(5-1). In all locations represented by the shaded areas in Fig. (5-1), $\chi_{eff}^{(2)}(x,z) \neq 0$ and everywhere else it is equal to zero.

Similarly, each spectral component $E_{op}(\omega,x,z)$ of the optical pump pulse spectrum is driven by a nonlinear polarization term $P_{op}(\omega,x,z)$ described in (5-6).

$$\begin{aligned} P_{op}(\omega,x,z) &= \varepsilon_0 \chi_{eff}^{(2)}(x,z).\int_0^\infty E_{op}(\omega+\Omega,x,z)E_{THz}{}^*(\Omega,x,z)d\omega \\ &+\varepsilon_0 \chi_{eff}^{(2)}(x,z).\int_0^\infty E_{op}(\omega-\Omega,x,z)E_{THz}(\Omega,x,z)d\omega \\ &-\frac{2k_{z0}\varepsilon_0 c^2}{\omega^2}\mathbf{F}\left\{\frac{\varepsilon_0\omega_0 n(\omega_0)^2 n_2(x,z)}{2}\left|E_{op}(t,x,z)\right|^2 E_{op}(t,x,z)\right\} \\ &-\frac{2k_{z0}\varepsilon_0 c^2}{\omega^2}\mathbf{F}\left\{j\frac{\varepsilon_0\omega_0 n(\omega_0)^2 n_2(x,z)}{2}\left[\left|E_{op}(t-t',x,z)\right|^2 \otimes h_r(t')\right]E_{op}(t,x,z)\right\} \end{aligned} \tag{5-6}$$

The first term in (5-6) is the analogue of the right hand side of (5-5). It corresponds to the OR process and signifies that an optical photon at angular frequency ω is created by an aggregate of DFG processes between optical photons at an angular frequency $\omega+\Omega$ and THz photons at angular frequency Ω. The impact of the various terms from (5-3a) on the nonlinear THz polarization term $P_{THz}(\Omega,x,z)$ is also seen here. The second term corresponds to an aggregate of SFG processes between optical photons at angular frequency ω-Ω and THz photons at angular frequency Ω. The third term in (5-6) represents the self-phase modulation of the optical pump pulse. Here, $E_{op}(t,x,z)$ is the time-domain electric field of the optical pump pulse and **F** represents the Fourier transform between time and frequency domains. The intensity dependent refractive index coefficient is $n_2(x,z)$ and has the same spatial profile as $\chi^{(2)}(x,z)$. The final term models Stimulated Raman Scattering. This term is very similar to the SPM term but includes the effects of a Raman gain lineshape given by $h_R(\omega')$.

We thus see how impacts on THz generation arising due to spatial variations in phase and amplitude of the optical electric fields in (5-3a) are captured by the nonlinear polarization terms.

5.1.3 Solving the 2-D non-linear wave equation using Fourier decomposition

In this section, we present our approach for solving the coupled system of nonlinear wave equations. The nonlinear polarization terms defined in (5-5) and (5-6) will drive the corresponding THz and optical fields. The nonlinear scalar wave equation for the evolution of the THz field $E_{THz}(\Omega,x,z)$ is presented in (5-7).

$$\nabla^2 E_{THz}(\Omega,x,z)+k^2(\Omega)E_{THz}(\Omega,x,z)=\frac{-\Omega^2}{\varepsilon_0 c^2}P_{THz}(\Omega,x,z) \tag{5-7}$$

In (5-7), $k(\Omega) = \Omega n(\Omega)/c$ is the wave number at the THz angular frequency Ω and $n(\Omega)$ is the corresponding refractive index at the THz frequency. Similar to (5-7), one can also write the corresponding wave equation for the optical fields at various angular frequencies ω in (5-8a).

$$\nabla^2 E_{op}(\omega,x,z) + k^2(\omega) E_{op}(\omega,x,z) = \frac{-\omega^2}{\varepsilon_0 c^2} P_{op}(\omega,x,z) \tag{5-8a}$$

A brute force solution of (5-8a) can be cumbersome because of the rapidly oscillating phase terms due to the large wave number of the optical field. In order to provide an efficient solution to the problem, we define a solution of the form $E_{op}(\omega,x,z) = A_{op}(\omega,x,z) e^{jk_{x0}(\omega).x} e^{-jk_{z0}(\omega).z}$. Here, $k_{x0}(\omega)$ and $k_{z0}(\omega)$ are wave vector components in the x and z directions of the (x,z) co-ordinate system, previously defined. Making this substitution into (5-8a), we obtain (5-8b) for the evolution of the optical field.

$$-2jk_{z0}\frac{\partial A_{op}(\omega,x,z)}{\partial z} + 2jk_{x0}\frac{\partial A_{op}(\omega,x,z)}{\partial x} + \frac{\partial^2 A_{op}(\omega,x,z)}{\partial x^2} = \frac{-\omega^2}{\varepsilon_0 c^2} P_{op}(\omega,x,z) e^{-jk_{x0}(\omega)x + jk_{z0}(\omega)z} \tag{5-8b}$$

Equation (5-7) drives the THz field which in turn affects the optical field via the nonlinear polarization term $P_{op}(\omega,x,z)$ defined in (5-6). However, the optical field directly influences the THz field via the nonlinear polarization term $P_{THz}(\Omega,x,z)$ defined in (5-5). Thus, (5-7) and (5-8a) form a coupled system of wave equations for THz and optical fields. An elegant solution to this system can be obtained via spatial Fourier decomposition. This effectively breaks up (5-7) and (5-8b) into a system of coupled 1-D first order differential equations which can be solved highly efficiently as will be shown below.

Applying Fourier transforms to both the left and right hand sides of (5-7) and we obtain (5-9a), which is nothing but a 1-D differential equation in z for $E_{THz}(\Omega,k_x,z)$. The evolution of $E_{THz}(\Omega,k_x,z)$ at each Ω and k_x can be governed separately.

$$\frac{\partial^2 E_{THz}(\Omega,k_x,z)}{\partial z^2} + \left(k^2(\Omega) - k_x^2\right) E_{THz}(\Omega,k_x,z) = \frac{-\Omega^2}{\varepsilon_0 c^2} P_{THz}(\Omega,k_x,z) \tag{5-9a}$$

Equation (5-9a) can be further simplified to (5-9b) by assuming a solution of the form $E(\Omega,k_x,z) = A(\Omega,k_x,z) e^{-jk_z(\Omega)z}$, where $k_z = \sqrt{k^2(\Omega) - k_x^2}$. The THz absorption coefficient at angular frequency Ω is given by $\alpha(\Omega)$.

$$\frac{\partial A(\Omega,k_x,z)}{\partial z} = \frac{-\alpha(\Omega)}{2} A(\Omega,k_x,z) - \frac{j\Omega^2}{(2k_z\varepsilon_0 c^2)} P^{(2)}(\Omega,k_x,z) e^{jk_z(\Omega).z} \tag{5-9b}$$

Similar to the spatial Fourier decomposition of (5-7), we Fourier transform both sides of (5-8b) to obtain the corresponding 1-D differential equation in z for the optical fields in (5-10a).

$$\frac{\partial A_{op}(\omega,k_x,z)}{\partial z} = -\frac{jk_{x0}(\omega)k_x}{k_{z0}(\omega)} A_{op}(\omega,x,z) + \frac{jk_x^2}{2k_{z0}} A_{op}(\omega,x,z) - \frac{\omega^2}{\varepsilon_0 c^2} P_{op}(\omega,k_x+k_{x0},z) e^{jk_{z0}(\omega)z} \tag{5-10a}$$

In (5-10a), the first term on the right hand side represents the oblique propagation of the optical field. The second term corresponds to the quadratic phase associated with a Gaussian beam and the final term is the nonlinear polarization term which includes all the cascading effects, SPM and SRS. Equations (5-9b) and (5-10a) form a system of coupled 1-D differential equations for each value of k_x. However, the numerical integration of (5-10a) requires a high spatial resolution because of the rapidly oscillating phase terms, i.e the first and second term of (5-10a). To circumvent this computational challenge, (5-10a) can be reduced to (5-10b) by noticing that $A_{op}(\omega,k_x,z)=\phi_{op}(\omega,k_x,z)e^{\left(-jk_{x0}(\omega)k_x/k_{z0}(\omega)+jk_x^2/2k_{z0}\right)z}$.

$$\frac{\partial\phi_{op}(\omega,k_x,z)}{\partial z}=-\frac{\omega^2}{\varepsilon_0 c^2}P_{op}(\omega,k_x-k_{x0},z)e^{j\left(k_{z0}(\omega)+\frac{k_{x0}(\omega)k_x}{k_{z0}(\omega)}-\frac{jk_x^2}{2k_{z0}}\right)z} \tag{5-10b}$$

In (5-10b), we see how the phase matching condition can be altered by the oblique propagation and finite size of the optical beam by examining the exponential factor. The dependence of the argument on k_x implies phase-matching condition will not be satisfied for all k_x values. Alternatively, optical field components at all values of k_x do not participate in the THz generation process. This is analogous to frequency dependent dispersion.

Equations (5-5), (5-6) and (5-9b) and (5-10b) are thus stepped through z, till we reach the end of the nonlinear crystal at $z=h\sin\alpha$

5.1.4 Calculating transmission and propagation of THz radiation

Once (5-5),(5-6),(5-9b) and (5-10b) are solved iteratively until the end of the nonlinear crystal, we obtain the THz electric field at Ω at the exit surface of the crystal. Next, we need to calculate the transmitted THz electric field. For this purpose we employ the standard Fresnel reflection coefficients as a function of the transverse momentum k_x. For THz field polarizations perpendicular to the plane of Fig.5-1, the Fresnel reflection coefficients are presented in (5-11). In [37], more specific reflection formulas for the case when the group velocity of optical and THz are very disparate are provided. However, in the case of tilted-pulse-fronts, this formula plays less of an important role as we are quite close to phase matching. So we can use the regular Fresnel formulae.

$$T(k_x)=\frac{2\sqrt{\frac{\Omega^2 n(\Omega)^2}{c^2}-k_x^2}}{\sqrt{\frac{\Omega^2 n(\Omega)^2}{c^2}-k_x^2}+\sqrt{\frac{\Omega^2}{c^2}-k_x^2}} \tag{5-11}$$

In order to calculate the THz field at a distance z_d away from the exit surface, we write a Huygen's integral without any approximation as shown in (5-12a). This equation can be re-written in terms of an Inverse Fourier Transform in (5-12b).

$$E(\Omega,x,z_d)=\int_{-\infty}^{\infty}A(\Omega,k_x,h\sin\alpha)T(k_x)e^{-j\left(k_0^2-k_x^2\right)^{1/2}z_d}e^{jk_x x}dk_x \tag{5-12a}$$

$$E(\Omega, x, z) = \mathbf{F}^{-1}\left(A(\Omega, k_x, h\sin\alpha)T(k_x)e^{-j\left(k_0^2 - k_x^2\right)^{1/2} z_d} \right) \tag{5-12b}$$

Thus using (5-1)-(5-12), we can model an arbitrary imaging system setup, combine it with a system of 2-D nonlinear coupled wave equations to solve for THz and optical fields and then calculate the transmitted THz radiation.

Despite the comprehensive modeling of the problem by (5-1)-(5-12), the computation is very efficient. Equations (5-9b) and (5-10b) effectively form a 1-D system of wave equations similar to [22] for each value of k_x. Therefore, the equations for various momentum values can be solved in parallel. The above system of equations was integrated using a 4th order Runge-Kutta method. The evaluation of Fourier transforms was accelerated by GPU parallelization (See Appendix D for further details).

5.2 Validation of the model

In this section, the developed model is validated against analytic theory and experiments. Simulations assume a simple grating and lens setup to create the tilted-pulse-fronts, in line with the experiments in [14], [21]. The full-width at half maximum (FWHM) pulse duration was assumed to be 0.5ps with a fluence of 20 mJ/cm^2, and a peak intensity of 40 GW/cm^2 was assumed as in [22]. The second order effective nonlinear coefficient was assumed to be $\chi_{eff}^{(2)}$ = 360 pm/V and the intensity dependent refractive index coefficient was n_2=10^{-15} cm^2/W. which is in the range of values specified by [30]. As a first step of verifying the accuracy of the developed model, we simulate the conversion efficiency as a function of the grating incidence angle (θ_i), grating to lens (s_1) and lens to crystal (s_2) distances. This is plotted in Fig. 5-2(a). It can be seen that an optimum conversion efficiency of 0.7% is obtained at s_1=60.89cm, s_2=36.84cm and θ_i=46.5^0. Analytic calculations for the optimal imaging conditions [17] are presented in Fig.5-2(b). Here, for an optimum pulse-front-tilt angle γ~63^0, the corresponding imaging distances very closely match the simulation results, i.e. s_1=60.19cm, s_2=37.23cm and θ_i=46.5^0. The experimentally obtained conversion efficiency (1.15%) is higher than the theoretical prediction, which is partially owed to uncertainties in certain material parameters [33]. This agreement in optimal imaging conditions is a strong validation of the developed model. In addition, the spatially averaged THz and optical spectra at the output facet of the crystal are presented in Figs. 5-2(c) and 5-2(d) respectively. The THz spectrum is centred at ~0.45 THz and is in close agreement with experimental measurements [21]. The optical spectrum is however broadened to a larger extent than the experimental results. One possible explanation for this is that the experimental measurements potentially suffer from clipping of the more divergent higher optical frequency components.

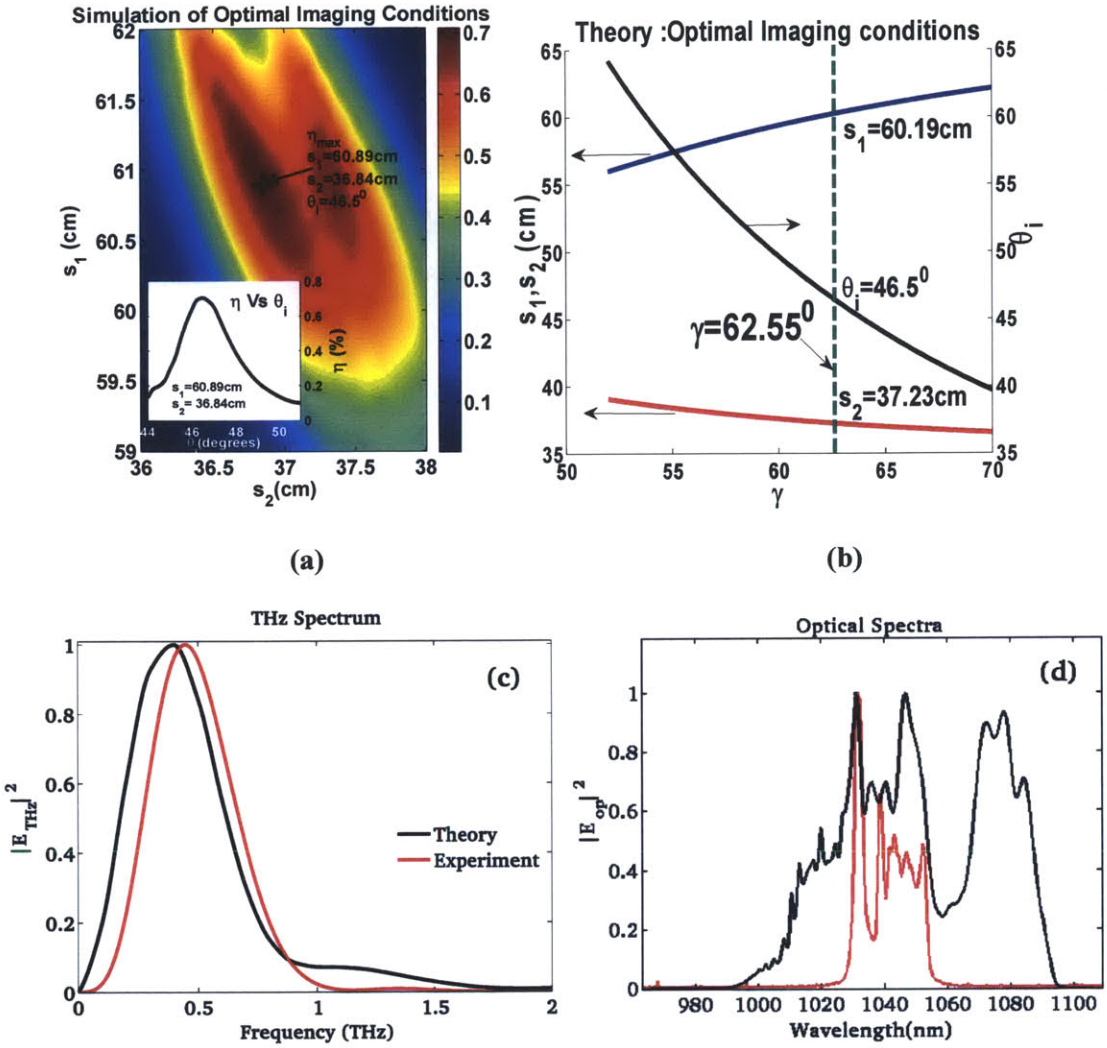

Figure 5-2(a): Simulation of conversion efficiency as a function of imaging conditions. The surface plot shows the conversion efficiency versus the imaging distances s1, s2 which are the lens to grating and lens to crystal distances respectively. The inset shows conversion efficiency versus incidence angle to diffraction grating. (b) Theoretical calculations of optimal imaging conditions for various pulse-front-tilt angles. For a pulse-front-tilt angle of ~63 degrees, the imaging conditions are in close agreement with the simulation results, validating the accuracy of the presented model. (c) The experimental and theoretically calculated spectra are presented. (d) The output optical spectrum is presented along with experimental results.

5.3 Understanding effective length in two dimensions

In the remainder of this paper, the procedures to optimize the conversion efficiency and the accompanying trade-offs are discussed. As a starting point for this discussion, it is useful to understand what the effective length in a 2-D geometry is since this is usually the parameter used to describe the previous 1-D models. In general, two factors determine what the optimal effective propagation length L_{eff} is. These include absorption and dispersion. A longer effective length leads to more absorption and dispersion. A short effective length would mean less of both but it would also translate to a smaller amount of THz generation. Therefore, there exists an optimum value where the amount of THz generation is sufficiently large but absorption and dispersion are sufficiently small.

In a 2-D non-collinear geometry, two parameters directly influence absorption and dispersion. These include the beam radius σ and the beam position h. These parameters were introduced previously but are presented for convenience once again in Fig. 5-3(a). The THz and optical beams propagate non-collinearly. Since, THz is generated only in the region where there is optical fluence, a larger value of h would mean that the overlap of the THz and optical beams would reduce and the THz would propagate over a longer absorptive region (i.e without optical fluence). Similarly, the optical beam would propagate longer distances which would mean they would suffer greater spectral broadening due to cascading effects and SPM. This in turn would make dispersive effects more acute. Therefore, one would expect that a larger value of h is necessarily more detrimental to THz generation. The exception to this would be when the optical pump beam is clipped or equivalently is not completely contained within the nonlinear region. Similarly, a larger value of beam radius σ would lead to a smaller overlap and a larger amount of absorption. Also a larger value of σ would lead to a greater amount of overlap, which would in turn lead to a greater amount of cascading and would accentuate dispersive effects further. These various effects are shown in Fig. 5-3(b)-(d). In Fig. 5-3(b), a beam with radius 2.5 mm, is placed 1.5 mm from the crystal apex. It can be seen how the THz and optical beams have good overlap which reduces absorptive effects and leads to a high conversion efficiency. In Fig. 5-3(c), the same beam is displaced further down the crystal. One sees that more THz absorption occurs leading to a large drop in conversion efficiency. In Fig. 5-3(d), a large beam size of 10mm radius is used which is very close to clipping the crystal. We see that only a small portion of the optical pump beam cross-section produces THz radiation. This is because, after initial THz generation, subsequent parts of the beam are spectrally broadened to an extent which prevents them from further generating THz. This has a powerful impact on the scaling of THz energies with large pump energies. If, the intensity is maintained constant and the beam size is enlarged, the conversion efficiency is not maintained as per earlier expectations due to the phase mismatch caused by the broadened optical spectrum. This places important limitations on the scaling of THz energies using large optical pump beam radii. An approach to circumvent this is to use an elliptically shaped pump beam with major axis perpendicular to the plane of the tilted-pulse-front (i.e in the y direction). Thus for a given intensity, both the beam position and beam radius have to be optimized in order to optimize conversion efficiency.

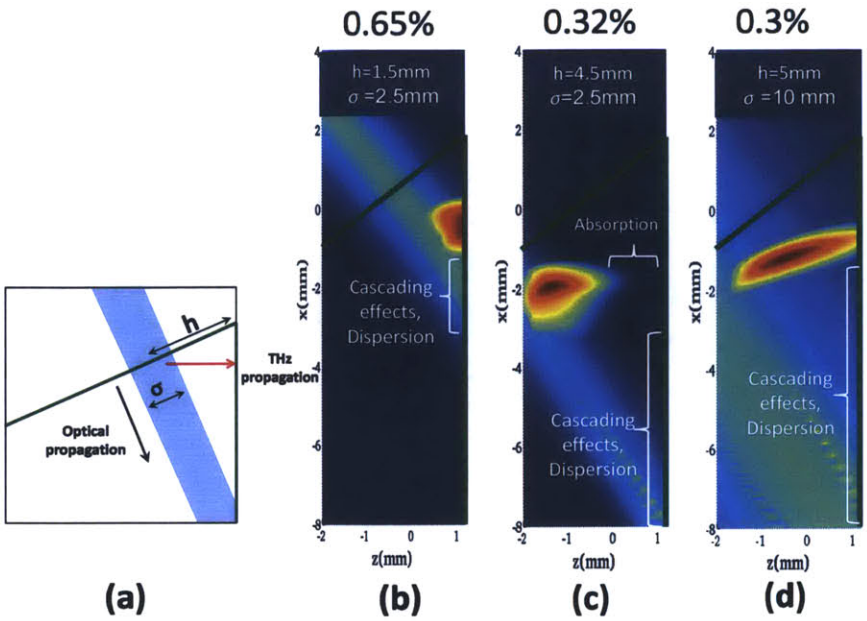

Figure 5-3(a). Effective length in two dimensions. The beam position h and beam position σ affect the amount of absorption and dispersion and affect the effective length in 2-D. Absorption is larger for larger h since there is less overlap with the optical beam, whereas σ is proportional to overlap and therefore reduces absorption. An increase in h or σ increase the effective propagation distance of the optical beam and therefore increase dispersive effects. Therefore for (b) small h and σ, there is minimal absorption (c) for large h and small σ, absorption increases and conversion efficiency drops (d) for large σ, only small portions of the beam are involved in THz generation, leading to an overall drop in conversion efficiency. This has important implications on the scaling of THz energies, by merely scaling beam size.

5.4 Considerations for optimizing conversion efficiency

Now that we have established how to think in terms of dispersion and absorption in terms of σ and h, it is useful to look at what factors influence absorption and dispersion. The main source of dispersion is bandwidth of the optical pump pulse, which in turn is dependent predominantly on spectral broadening by cascading effects. This broadening increases with both initial optical pump intensity as well as initial bandwidth. Thus, when either optical pump intensity or bandwidth are changed, the effect of dispersion changes which in turn affects the optimal effective lengths or equivalently, the corresponding optimal values of beam radius and beam position.

Changes in absorption and dispersion will change the optimal effective length which in turn affects the optimal h and optimal σ. However, dispersion is affected by both the intensity as well as the bandwidth of the input optical pulse and therefore for different intensities/bandwidth, the setup has to be optimized differently. Equivalently, the optimal intensities/ bandwidths are different for different beam sizes and different temperatures. This makes optimization of the THz generation system a complex problem.

Suppose the peak intensity is increased, this would lead to a faster rate of THz generation, which would in turn cause spectral broadening to occur faster. Therefore, the effects of dispersion would be accentuated over a shorter distance compared to before and the optimal effective length would reduce. This can be achieved by a reduction of beam position or beam size, while keeping the peak intensity constant.

In Fig.5-4, we plot the conversion efficiency as a function of the peak intensity of the optical pump pulse for different beam positions *h*. It can be seen that the shape of the curves is different for different beam positions. Each curve shows a different saturation intensity or conversely, there is an optimal beam position for a given peak intensity value. This could be one reason why, various experimental report very different saturation curves. Thus, in optimizing conversion efficiency, a careful optimization of the experimental setup is required.

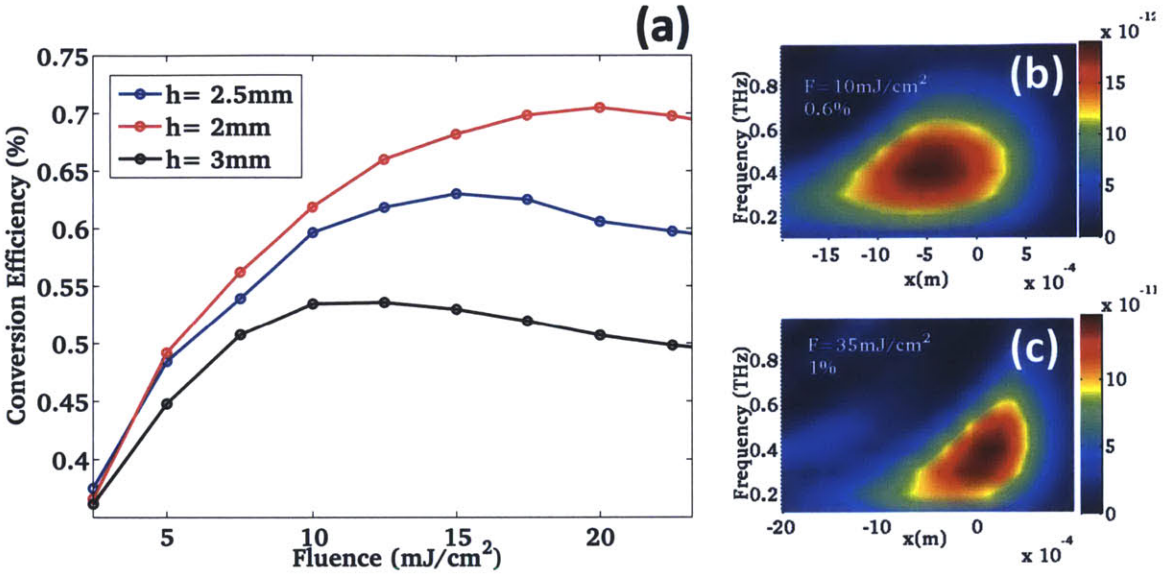

Figure 5-4 (a) Conversion efficiency saturation curves for different beam positions *h*. The saturation energy/fluence is dependent on the beam position. (b) While conversion efficiency may increase with increasing intensity, other detrimental effects such as significant spatial-chirp of the THz spectrum also occur. Therefore, optimization of such systems must consider other aspects of THz radiation while optimizing the setup.

In the previous two sections, we have illustrated the concept of effective length in 2-D and how it translates to the complexity of optimizing the experiment. The next question, we pose as a conclusion to this thesis is whether optimizing conversion efficiency should be the only priority in the construction of such setups. Evidence for this is shown in Figs. 5-4(b) and 5-4(c). It is seen that while the intensity does increase conversion efficiency, it also introduces a large spatial-chirp in the THz spectrum. Such a spatial chirp is detrimental to beam transport, focusing and therefore would be perhaps less useful than one with marginally lower conversion efficiency but superior beam characteristics.

6. Conclusion and future work

In the pursuit of optical-to-THz conversion efficiencies on the order of 10%, pulse energies of ~ 10 mJ and pulse durations in the range of a few ps to few hundred picoseconds, we turned to the approach of optical rectification via tilted-pulse-fronts in lithium niobate. While earlier theory predicted conversion efficiencies as high as 10%, experimental results have been signficantly smaller. This led to a re-formulation of the theory in greater detail. The main improvement was the consideration of the coupled interaction between the optical pump and generated THz radiation in two spatial dimensions. This revealed that a simultaneous broadening of the optical pump pulse in momentum and frequency occurs as a natural consequence of THz generation. This leads to a rapid spatio-temporal break-up of the optical pump pulse. The implications of this new physical insight are as follows.

(i) Since THz generation necessarily leads to this spatio-temporal break-up, the optical rectification process is inherently a self-limiting process.

(ii) The effective length of THz generation reduces to a ~few mm which drastically reduces the predicted conversion efficiency.

(iii) The reduction of the effective length also implies that scaling of THz energy to very large beam sizes will lead to a drop in conversion efficiency, which had not been anticipated previously. This can be circumvented by the use of an elliptically shaped beam, with major axis perpendicular to the plane in which the pulse front is tilted.

(iv) The spatio-temporal break-up of the optical pulse causes large spatio-temporal distortions in the THz properties. This affects the beam transport and focusing properties of the THz pulse.

The above insights into THz generation pose important questions which shall be the emphasis of future work. Firstly, it would be important to find out what the maximum achievable conversion efficiency in lithium niobate is, under any arbitrary circumstance. Next, methods to compensate for detrimental dispersive effects have to be considered. Operation at longer pump-wavelengths to reduce spectral broadening is yet another important consideration. Then there is the combination of these various approaches in tandem. The thesis thus puts the solution to the problem on the right path, to deviate from existing approaches and to re-think the strategy to push the frontier of high-field THz generation.

7. Appendix A: Tilted-pulse-fronts

First, one can show how an angularly dispersed pulse results in a tilted-pulse-front. Note that the converse is not necessarily true. A tilted-pulse-front can also result from a spatially chirped pulse. A detailed discussion of various spatio-temporal distortions and their correlation to pulse-front-tilts is provided in [23]. Here, the endeavor is purely illustrative and not meant to be exhaustive.

$$
\begin{aligned}
E(\omega,x,z) &= E_0 e^{-\frac{\tau^2(\omega-\omega_0)^2}{4}} e^{-\frac{x^2}{\sigma^2}} e^{-j\left[k_0+v_g^{-1}(\omega-\omega_0)\right]z} e^{-jk_0\beta(\omega-\omega_0)x} \\
E(t,x,z) &= e^{j\omega_0 t}\int_{-\infty}^{\infty} E_0 e^{-\frac{\tau^2\omega'^2}{4}} e^{-\frac{x^2}{\sigma^2}} e^{-jk_0 z} e^{-jk_0\beta\omega' x} e^{-jv_g^{-1}\omega' z} e^{j\omega' t} d\omega' \\
&= e^{j\omega_0 t} e^{-jk_0 z}\int_{-\infty}^{\infty} E_0 e^{-\frac{\tau^2\omega'^2}{4}} e^{-\frac{x^2}{\sigma^2}} e^{j\omega'(t-v_g^{-1}z-k_0\beta x)} d\omega' \\
\Rightarrow E(t,x,z) &= E_0 e^{-\frac{(t-v_g^{-1}z-k_0\beta x)^2}{\tau^2}} e^{-\frac{x^2}{\sigma^2}} e^{j(\omega_0 t-k_0 z)}
\end{aligned}
\tag{A-1}
$$

Inspecting (A-1), we see that the all points with the same value of $t-v_g^{-1}z-k_0\beta x$ have the same intensity. This describes an inclined or tilted intensity profile. Second, the phase velocity is still z directed, indicating that the phase fronts are still perpendicular to the propagation direction. Based on our definition of the angle γ in Fig.1-1, the angle γ is determined by the derivative of z with respect to x.

Therefore, $\frac{dz}{dx} = k_0\beta v_g = \tan\gamma$. However, β is nothing but the angular dispersion $\left.\frac{d\theta}{d\omega}\right|_{\omega_0}$. Therefore, we have the following relationship between the pulse-front-tilt angle and angular dispersion.

$$
-\lambda_0 \frac{n(\lambda_0)}{n_g(\lambda_0)} \frac{d\theta}{d\lambda} = \tan\gamma \tag{A-2}
$$

Using, (A-2) we can derive the group-velocity-dispersion (GVD-AD) due to angular dispersion used in Chapter 4. Here, $\vec{\beta}(\omega)$ is the propagation vector, propagating at an angle $\theta \sim 0$. The corresponding second derivative can then be explicitly calculated, and by substituting (A-2), (A-3) is obtained.

$$
\begin{aligned}
\vec{\beta}(\omega) &= k(\omega)\cos\theta\hat{a}_z + k(\omega)\sin\theta\hat{a}_x \\
\left.\frac{d^2\beta(\omega)}{d\omega^2}\right|_{\omega_0} &= k(\omega)\left(\frac{d\theta}{d\omega}\right)^2 = -n(\lambda_0)\left(\frac{d\theta}{d\lambda}\right)^2 \frac{\lambda_0^3}{2\pi c} \\
\left.\frac{d^2\beta(\omega)}{d\omega^2}\right|_{\omega_0} &= -\frac{n_g^2(\lambda_0)}{n(\lambda_0)\omega_0}\tan^2\gamma
\end{aligned}
\tag{A-3}
$$

8. Appendix B: Energy conservation in optical rectification

The one-dimensional equations for THz generation by optical rectification are described below in (B-1) to (B-2).

$$\frac{dA_{op}(\omega)}{dz} = -j\frac{\omega^2\chi_{eff}^{(2)}}{2k(\omega)}\int_0^\infty A_{op}(\omega+\Omega)A_{THz}{}^*(\Omega)e^{-j[k(\omega+\Omega)-k(\Omega)-k(\omega)]z}d\Omega - j\frac{\omega^2\chi_{eff}^{(2)}}{2k(\omega)}\int_0^\infty A_{op}(\omega-\Omega)A_{THz}(\Omega)e^{-j[k(\omega+\Omega)-k(\Omega)-k(\omega)]z}d\Omega \tag{B-1}$$

$$\frac{dA_{THz}(\Omega)}{dz} = -j\frac{\Omega^2\chi_{eff}^{(2)}}{2k(\Omega)}\int_0^\infty A_{op}(\omega+\Omega)A_{op}{}^*(\omega)e^{-j[k(\omega+\Omega)-k(\Omega)-k(\omega)]z}d\omega \tag{B-2}$$

The total Poynting vector is written below in (B-3).

$$S_{tot}(z) = \frac{1}{2}\int_0^\infty \frac{k(\omega)}{\omega\mu_0}\left|A_{op}(\omega,z)\right|^2 d\omega + \frac{1}{2}\int_0^\infty \frac{k(\Omega)}{\Omega\mu_0}\left|A_{THz}(\Omega,z)\right|^2 d\Omega \tag{B-3}$$

To check for energy conservation, the spatial derivative of the Poynting vector must vanish in the absence of any energy dissipative mechanisms. The spatial derivative is written in (B-4).

$$\begin{aligned}\frac{dS_{tot}(z)}{dz} &= \frac{1}{2}\int_0^\infty \frac{k(\omega)}{\omega\mu_0}\left\{A_{op}(\omega,z)\frac{dA_{op}{}^*(\omega,z)}{dz} + A_{op}{}^*(\omega,z)\frac{dA_{op}(\omega,z)}{dz}\right\}d\omega \\ &+\frac{1}{2}\int_0^\infty \frac{k(\Omega)}{\Omega\mu_0}\left\{A_{THz}(\Omega,z)\frac{dA_{THz}{}^*(\Omega,z)}{dz} + A_{THz}{}^*(\Omega,z)\frac{dA_{THz}(\Omega,z)}{dz}\right\}d\Omega\end{aligned} \tag{B-4}$$

Substituting (B-1) ad (B-2) in (B-4), we have the following expressions in (B-5) and (B-6) for the spatial derivatives of the optical and THz radiation respectively. Here *cc* is the complex conjugate of the presented expression.

$$\begin{aligned}&\int_0^\infty\int_0^\infty -j\frac{\omega\chi_{eff}^{(2)}}{2\mu_0}A_{op}{}^*(\omega)A_{op}(\omega+\Omega)A_{THz}{}^*(\Omega)e^{-j[k(\omega+\Omega)-k(\Omega)-k(\omega)]z}d\Omega d\omega + cc \\ &+\int_0^\infty\int_0^\infty -j\frac{\omega\chi_{eff}^{(2)}}{2\mu_0}A_{op}{}^*(\omega)A_{op}(\omega-\Omega)A_{THz}(\Omega)e^{-j[k(\omega-\Omega)+k(\Omega)-k(\omega)]z}d\Omega d\omega + cc\end{aligned} \tag{B-5}$$

$$\int_{-\infty}^\infty\int_{-\infty}^\infty -j\frac{\Omega\chi_{eff}^{(2)}}{2\mu_0}A_{THz}{}^*(\Omega)A_{op}(\omega+\Omega)A_{op}{}^*(\omega)e^{-j[k(\omega+\Omega)-k(\Omega)-k(\omega)]z}d\omega d\Omega + cc \tag{B-6}$$

Simple algebraic manipulation of the second term of (B-5), i.e, making the transformation of variables from ω to $\omega+\Omega$, allows for re-casting (B-5) as (B-7).

$$\begin{aligned}&\int_0^\infty\int_0^\infty -j\frac{\omega\chi_{eff}^{(2)}}{2\mu_0}A_{op}{}^*(\omega)A_{op}(\omega+\Omega)A_{THz}{}^*(\Omega)e^{-j[k(\omega+\Omega)-k(\Omega)-k(\omega)]z}d\Omega d\omega + cc \\ &+\int_0^\infty\int_0^\infty j\frac{(\omega+\Omega)\chi_{eff}^{(2)}}{2\mu_0}A_{op}(\omega+\Omega)A_{op}{}^*(\omega)A_{THz}{}^*(\Omega)e^{-j[k(\omega+\Omega)-k(\omega)-k(\Omega)]z}d\Omega d\omega + cc\end{aligned} \tag{B-7}$$

Note that the sum of (B-6) and (B-7) is equal to zero and hence the conservation of energy is established.

9. Appendix C: Numerical convergence of depleted model

A 4th order Runge-Kutta method was used for numerical integration. Euler integration approaches do not work sufficiently well for propagation over long distances or for the 2-D implementations. For 2-D geometries, the problem is relatively stiff and requires very fine spatial and temporal resolution, due to simultaneous broadening in spectral and momentum domains. A number of *n(n+1)* Runge-Kutta methods were tried, i.e. 4(5), 5(6), 6(7) and 7(8). However, the 4th order method appears to work better even compared to the 7(8) approaches. Here we present the numerical algorithm for the 4th order Runge-Kutta implementation in (C-1) through (C-5).

$$l_{THz(op)}\Big|^{\Omega(\omega),k_x,1} = \Delta z \cdot f_{THz(op)}\left(A_{THz}\Big|^{\Omega,k_x,z}, A_{op}\Big|^{\omega,k_x,z}\right) \tag{C-1}$$

$$l_{THz(op)}\Big|^{\Omega(\omega),k_x,2} = \Delta z \cdot f_{THz(op)}\left(A_{THz}\Big|^{\Omega,k_x,z} + \frac{l_{THz}\Big|^{\Omega,k_x,1}}{2}, A_{op}\Big|^{\omega,z} + \frac{l_{op}\Big|^{\omega,k_x,1}}{2}\right) \tag{C-2}$$

$$l_{THz(op)}\Big|^{\Omega(\omega),k_x,3} = \Delta z \cdot f_{THz(op)}\left(A_{THz}\Big|^{\Omega,k_x,z} + \frac{l_{THz}\Big|^{\Omega,k_x,2}}{2}, A_{op}\Big|^{\omega,z} + \frac{l_{op}\Big|^{\omega,k_x,2}}{2}\right) \tag{C-3}$$

$$l_{THz(op)}\Big|^{\Omega(\omega),k_x,4} = \Delta z \cdot f_{THz(op)}\left(A_{THz}\Big|^{\Omega,k_x,z} + l_{THz}\Big|^{\Omega,k_x,3}, A_{op}\Big|^{\omega,z} + l_{op}\Big|^{\omega,k_x,3}\right) \tag{C-4}$$

$$A_{THz(op)}\Big|^{\Omega(\omega),k_x,z+\Delta z} = A_{THz(op)}\Big|^{\Omega(\omega),k_x,z} + \frac{1}{6}\left(l_{THz(op)}\Big|^{\Omega(\omega),k_x,1} + 2l_{THz(op)}\Big|^{\Omega(\omega),k_x,2} + 2l_{THz(op)}\Big|^{\Omega(\omega),k_x,3} + l_{THz(op)}\Big|^{\Omega(\omega),k_x,4}\right) \tag{C-5}$$

For the simulation parameters described in Chapter 4, we propagate over a distance of 4mm and notice the convergence of results at a relatively sparse resolution of 10 μm. The THz and optical spectra and phases are plotted below in Fig. 9-1.

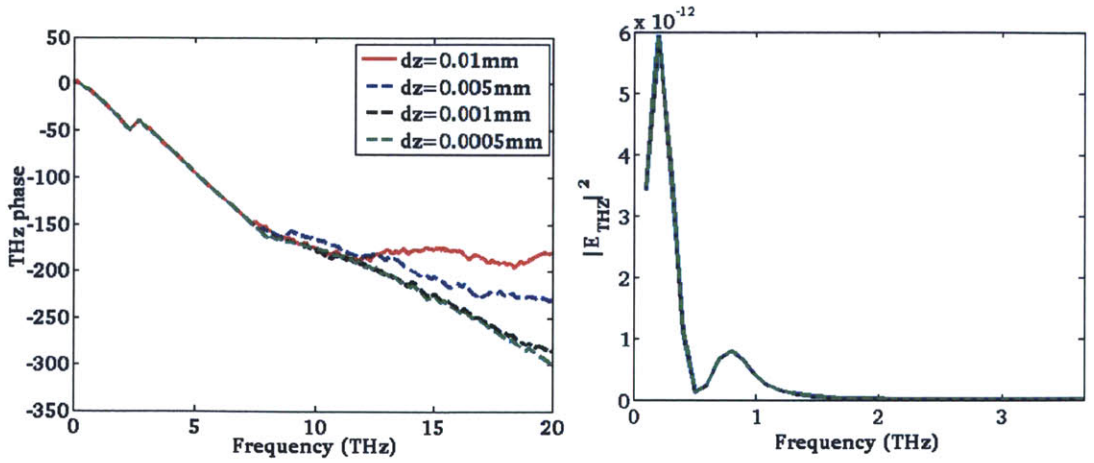

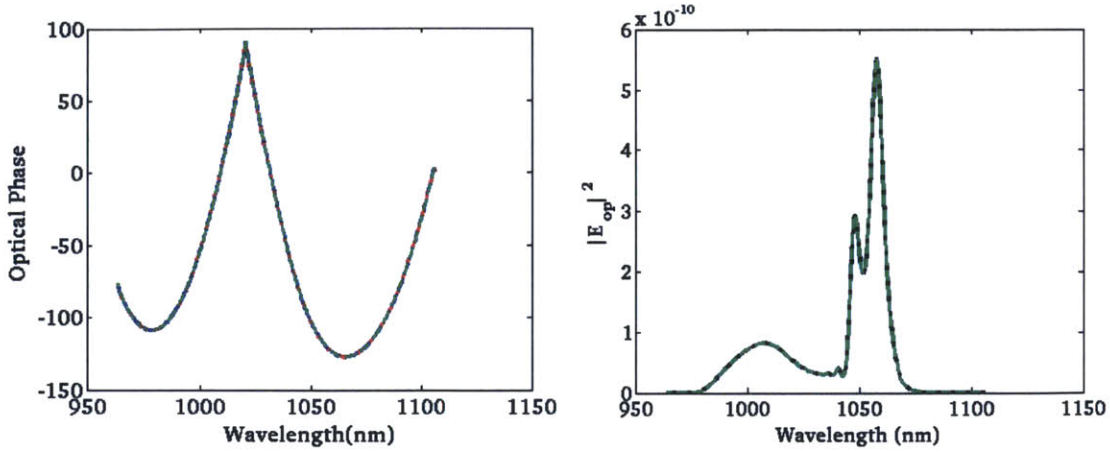

Figure 9-1. Numerical convergence of simulation for (a) THz spectral phase. (b) THz spectral magnitude.(c) Optical phase and (d) Optical spectrum for propagation over a distance of 4mm in Lithium Niobate.

10. Appendix D: Notes on 2-D implementation

Vectorizing calculations

MATLAB is not well suited in handling for-loops. Since we have a number of variables which are functions of frequency/time, x/momentum (k_x) and z, looping structures must be minimized. Since the point of spatial Fourier decomposition is to enable a parallel solution, upto 2 dimensions can be solved in parallel and only a single looping structure (looping through z) would be required. Therefore all operations in ω and k_x were vectorized.

Representing Nonlinear Polarization terms as Fourier Transforms

The nonlinear polarization term driving the THz field can be written as follows. Note that, here we switch to an integral from $-\infty$ to ∞ instead of the previous definitions where it was a summation from 0 to ∞. This lends itself to being calculated via Fourier transforms as will be shown below.

$$P(\Omega,x,z)=\varepsilon_0\chi_{eff}^{(2)}(x,z)\int_{-\infty}^{\infty}E_{op}(\omega+\Omega,x,z)E_{op}{}^{*}(\omega,x,z)\,\mathrm{d}\omega \tag{D-1}$$

Algebraic manipulation leads to (D-1) being written as (D-2).

$$\begin{aligned}P(\Omega,x,z)&=\varepsilon_0\chi_{eff}^{(2)}(x,z)\int_{-\infty}^{\infty}\int_{-\infty}^{\infty}E_{op}(t,x,z)e^{-j(\omega+\Omega)t}dt\cdot E^{*}(\omega,x,z)d\omega\\&=\varepsilon_0\chi_{eff}^{(2)}(x,z)\int_{-\infty}^{\infty}E_{op}(t,x,z)\left\{\int_{-\infty}^{\infty}e^{-j\omega t}E(\omega,x,z)d\omega\right\}^{*}e^{-j\Omega t}dt\end{aligned} \tag{D-2}$$

Finally, (D-2) can be expressed in terms of Fast-Fourier-Transforms (FFT) and Inverse-Fast-Fourier-Transforms (IFFT) below in (D-3). Only the latter half of the calculated array will be used since the first half does not correspond to a physical frequency.

$$P(\Omega,x,z)=\varepsilon_0\chi_{eff}^{(2)}(x,z)\int_{-\infty}^{\infty}E_{op}(t,x,z)E_{op}{}^{*}(t,x,z)e^{-j\Omega t}dt=\varepsilon_0\chi_{eff}^{(2)}\mathrm{FFT}(|\,\mathrm{IFFT}[E_{op}(\omega,x,z)]\,|^2) \tag{D-3}$$

Similarly, the nonlinear polarization term driving is written in (D-4) and simplified to (D-5) on the same lines as (D-1) to (D-3). Once again, the physical THz frequencies only extend from 0 to ∞. However, for ease of computation in terms of Fourier Transforms, an integral from $-\infty$ to ∞ is considered. It follows then that the THz field for negative frequencies is defined to be the complex conjugate of the positive frequencies, i.e. $E(-\Omega)=E^{*}(\Omega)$.

$$\begin{aligned}P(\omega,x,z)&=\varepsilon_0\chi_{eff}^{(2)}(x,z)\int_{0}^{\infty}E_{op}(\omega-\Omega,x,z)E_{THz}(\Omega,x,z)\,\mathrm{d}\Omega+\varepsilon_0\chi_{eff}^{(2)}\int_{0}^{\infty}E_{op}(\omega+\Omega,x,z)E_{THz}{}^{*}(\Omega,x,z)\,\mathrm{d}\Omega\\&=\varepsilon_0\chi_{eff}^{(2)}\int_{-\infty}^{\infty}E_{op}(\omega+\Omega,x,z)E_{THz}{}^{*}(\Omega,x,z)\,\mathrm{d}\Omega\end{aligned} \tag{D-4}$$

$$P(\omega,x,z)=\varepsilon_0\chi_{eff}^{(2)}(x,z)\mathrm{FFT}\{\mathrm{IFFT}[\mathrm{E}_{op}(\omega,x,z)].(\mathrm{IFFT}[\mathrm{E}_{THz}(\Omega,x,z)]^*)\} \quad \text{(D-5)}$$

The above implementation significantly speeds up computations of the nonlinear polarization terms. The validity of calculating transforms via this approach is seen in their convergence with explicit calculations of (D-1) and (D-4) in Fig.10-1.

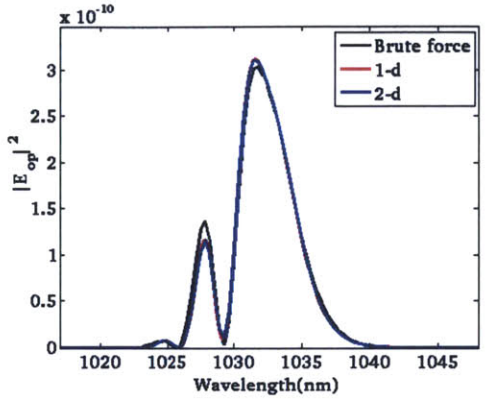

Figure 10-1 : Convergence of optical spectra calculations via brute-force (D-1) and (D-4) and Fourier transform approaches (D-3) and (D-5). The propagation length was 2mm. Beyond this propagation length, the brute-force approach is numerically too cumbersome to evaluate.

Notes on Fourier Transforms

In the actual MATLAB implementation, applying FFTSHIFT twice does not undo the action of the first operation in all cases. Since centering the spectrum is necessary for any operations on the spectrum but subsequent operation may require reverting to the time domain and vice-versa, the following definitions for the Fourier transform were used to ensure seamless universal operation.

FFT_custom = FFTSHIFT{FFT{IFFTSHIFT{}}}

IFFT_custom = FFTSHIFT{IFFT{IFFTSHIFT{}}}

Notice that the two operations are inverses of each other.

Parallelization and GPU implementation

GPU operation significantly speeds up the computations of Fourier transforms. A 4x improvement in speed is obtained with appropriate GPU implementation. One shortcoming is that not all the data may be easily retrieved due to the limited size of the GPU memory. One approach to circumvent this issue is to periodically extract the information from the GPU memory. However, this incurs a communication overhead. Therefore, there is an optimal number of data extraction processes that need to be carried out.

Dispersive Ray Pulse Matrices for common elements

Propagation through material of refractive index $n(\omega)$ and length L

$$\begin{bmatrix} 1 & L/n(\omega) & 0 \\ 0 & 1 & 0 \\ 0 & 0 & 1 \end{bmatrix} \tag{D-6}$$

Diffraction grating

The 6x6 matrix for the diffraction grating is presented below. The derivation follows straight forwardly from the grating equation, i.e $\sin\theta_i + \sin\theta_d(\omega) = \frac{p\omega}{2\pi c}$, where p is the spacing between grating lines.

$$\begin{bmatrix} A & 0 & 0 \\ 0 & D & F(\omega) \\ 0 & 0 & 1 \end{bmatrix} \tag{D-7}$$

$$F_0 = \frac{-2\pi c n_{\omega_0}{}^2(\omega - \omega_0)}{\Delta\omega^2 \cos\theta_d} \tag{D-8}$$

$$A = \frac{\cos\theta_d}{\cos\theta_i}\left(1 - \frac{\tan\theta_d F_0}{n(\omega_0)}\right) \tag{D-9}$$

$$D = \frac{\cos\theta_i}{\cos\theta_d}\left(1 - \frac{\tan\theta_d F_0}{n(\omega_0)}\right) \tag{D-10}$$

$$\begin{aligned} F_1 &= F_0\left(1 - \frac{(\omega - \omega_0)}{\omega_0} + \frac{1}{2}\tan\theta_d F_0\right) \\ F_2 &= F_0\left(\left(\frac{\omega - \omega_0}{\omega_0}\right)^2 + \frac{1}{2}\tan\theta_d F_1 + \frac{F_0^2}{6}\right) \\ F(\omega) &= F_0 + F_1 + F_2 \end{aligned} \tag{D-11}$$

11. References

[1] H. Chapman et al, "Femtosecond x-ray protein nanocrystallography," *Nature,* vol. 470, pp. 73-77, 2011.

[2] American Heart Association, " Executive Summary: Heart Disease and Stroke Statistics—2013 Update," 2013.

[3] J. C. Breneman, "Electron Beam Therapy," in *Radiation Treatment and Radiation Reactions in Dermatology,* Berlin Heidelberg, Springer, 2004, pp. 89-96.

[4] A. Zewail, "4D ultrafast electron diffraction, crystallography, and microscopy," *Annual Reviews in Physical Chemistry,* vol. 57, pp. 65-103, 2006.

[5] L. J. Wong, A. Fallahi and F. X. Kaertner, "Compact electron acceleration and bunch compression in THz waveguides," *Optics Express,* vol. 21, no. 8, pp. 9792-9806, 2013.

[6] H. Y. Hwang, S. Fleischer, N. C. Brandt, B. G. Perkins Jr, M. Liu, K. Fan, A. Sternbach, X. Zhang, R. D. Averitt and K. A. Nelson, "A review of non-linear terahertz spectroscopy with ultrashort tabletop-laser pulses," *Journal of modern optics,* vol. 10.1080/09500340.2014.918200, 2014.

[7] P. H. Siegel, "Terahertz Technology," *IEEE Transactions on Microwave Theory and Techniques,* vol. 50, pp. 910-928, 2002.

[8] M. Tonouchi, "Cutting-edge terahertz technology," *Nature Photonics,* vol. 1, pp. 97-105, February 2007.

[9] B. S. Williams, "Terahertz Quantum Cascade Lasers," *Nature Photonics,* vol. 1, pp. 517-519, September 2007.

[10] J. H. Booske, J. R. Dobbs, C. D. Joye, C. L. Kory, G. R. Neil, G.-S. Park, J. Park and R. J. Temkin, "Vacuum Electronic High Power Terahertz Sources," *IEEE Transactions on Terahertz Science and Technology,* vol. 1, no. 1, pp. 54-75, September 2011.

[11] K. L. Yeh, M. C. Hoffmann, J. Hebling and K. A. Nelson, "Generation of 10 uJ ultrashort THz pulses by optical rectification," *Applied Physics Letters,* vol. 90, p. 171121, 2007.

[12] J. Hebling, G. Almasi, I. Z. Kozma and J. Kuhl, "Velocity matching by pulse front tilting for large area THz pulse generation," *Optics Express,* vol. 21, no. 10, pp. 1161-1166, 2002.

[13] H. Hirori, A. Doi, F. Blanchard and K. Tanaka, "Single-cycle terahertz pulses with amplitudes exceeding 1MV/cm," *Applied Physics Letters,* vol. 98, p. 091106, 2011.

[14] S. W. Huang, E. Granados, W. R. Huang , K. H. Hong, L. Zapata and F. X. Kaertner, "High conversion efficiency, high energy terahertz pulses by optical rectification," *Optics Letters,* vol. 38, no. 5, pp. 796-798, 2013.

[15] J. A. Fulop, L. Palfalvi, M. Hoffmann and J. Hebling, "Efficient generation of THz Pulses with 0.4 mJ Energy," in *Conference on Lasers and Electro-Optics*, San Jose, 2014.

[16] J. A. Fulop, L. Palfalvi, M. Hoffmann and J. Hebling, "Towards generation of mJ-level ultrashort THz pulses by

optical rectification," *Optics Express,* vol. 19, no. 16, pp. 15090-15097, 2011.

[17] J. A. Fulop, L. Palfalvi, G. Almasi and J. Hebling, "Design of high-energy terahertz sources based on optical rectification," *Optics Express,* vol. 18, no. 12, pp. 12311-12327, 2010.

[18] S. Bodrov, A. Murzanev, Y. A. Sergeev, Y. A. Malkov and A. N. Stepanov, "Terahertz generation by tilted pulse fronts in weakly and strongly nonlinear regimes," *Applied Physics Letters,* vol. 2013, p. 251103, 103.

[19] M. Bakunov, S. Bodrov and E. Maskovich, "Terahertz generation with titled-front laser pulses : dynamic theory for low absorbing crystals," *Journal of optical society of america B,* vol. 28, no. 7, pp. 1724-1734, 2011.

[20] M. Jewariya, M. Nagai and K. Tanaka, "Enhancement of terahertz wave generation by cascaded chi_2 processes," *Journal of Optical society of America B,* vol. 26, no. 9, pp. A101-A106, 2009.

[21] W. R. Huang, S. W. Huang, E. Granados, K. Ravi, K. H. Hong, L. Zapata and F. X. Kaertner, "Highly efficient terahertz pulse generation by optical rectification in stoichiometric and cryo-cooled congruent lithium niobate," *Journal of Modern Optics,* vol. 10.1080/09500340.2013.868547, 2014.

[22] K. Ravi, W. R. Huang, S. Carbajo, X. Wu and F. X. Kaertner, "Limitations to THz generation by optical rectification using tilted pulse fronts," *Optics Express,* vol. 22, no. 17, pp. 20239-20251, 2014.

[23] S. Akturk, X. Gu, E. Zeek and R. Trebino, "Pulse-front tilt caused by spatial and temporal chirp," *Optics Express,* vol. 12, no. 19, pp. 4399-4410, 2004.

[24] O. E. Martinez, "Matrix formalism for pulse compressors," *IEEE Journal of Quantum Electronics,* vol. 24, no. 12, pp. 2530-2536, 1989.

[25] F. Blanchard, X. Ropagnol, H. Hafez, H. Razavipour, M. Bolduc, R. Morandotti, T. Ozaki and D. G. Cooke, "Effect of extreme pump pulse reshaping on intense terahertz emission in lithium niobate at multimilliJoule pump energies," *Optics Letters,* vol. 39, no. 15, pp. 4333-4336, 2014.

[26] K. Vodopyanov, "Optical generation of narrow-band terahertz packets in periodically-inverted electro-optic crystals : conversion efficiency and optimal laser format," *Optics Express,* vol. 14, no. 6, pp. 2263-2276, 2006.

[27] R. Boyd, Nonlinear Optics, Academic Press, 2005.

[28] C. Vicario, B. Monoszlai, C. S. Lombosi, A. Mareczko, A. Courjaud, J. A. Fulop and C. P. Hauri, "Pump pulse width and temperature effects in lithium niobate for efficient THz generation," *Optics Letters,* vol. 38, no. 24, pp. 5373-5376, 2013.

[29] X. Wu, S. Carbajo, K. Ravi, F. Ahr, G. Cirmi, Y. Zhou, O. Mucke and F. Kaertner, "Terahertz Generation in Lithium Niobate Driven by Ti:Sapphire Laser Pulses and its Limitations," *ArXiv,* vol. 1406.4949, 2014.

[30] T. Fujiwara, M. Takahashi, M. Ohama, A. J. Ikushima, Y. Furukawa and K. Kitamura, "Comparison of electro-optic effect between stoichiometric and congruent lithium niobate," *Electronics Letters,* vol. 35, no. 6, pp.

499-501, 1999.

[31] R. DeSalvo, A. A. Said, D. J. Hagan, E. W. Van Stryland and M. Sheik-Bahe, "Comparison of electro-optic effect between stoichiometric and congruent lithium niobate," *IEEE Journal of Quantum Electronics,* vol. 32, no. 8, pp. 1324-1333, 1996.

[32] C. R. Phillips, C. Langrock, J. S. Pelc, M. M. Fejer, I. Hartl and M. E. Fermann, "Supercontinuum generation in quasi-phasematched waveguides," *Optics Express,* vol. 19, no. 20, pp. 18754-18773, 2011.

[33] L. Palfalvi, J. Hebling , J. Kuhl, A. Peter and K. Polgar, "Temperature dependence of the absorption and refraction of Mg-doped congruent and stoichiometric lithium niobate in the THz range," *Journal of Applied Physics,* vol. 97, p. 123505, 2005.

[34] M. C. Hoffmann, K. L. Yeh, J. Hebling and K. A. Nelson, "Efficient terahertz generation by optical rectification at 1035nm," *Optics Express,* vol. 15, no. 18, pp. 11707-11713, 2007.

[35] B. S. Wherrett, "Scaling rules for multiphoton interband absorption in semiconductors," *Journal of Optical Society of America B,* vol. 1, no. 1, pp. 67-72, 1984.

[36] O. E. Martinez, "Matrix Formalism for Pulse Compressors," *IEEE Journal of Quantum Electronics,* vol. 24, p. 2530, 1988.

[37] M. I. Bakunov, A. V. Maslov and S. B. Bodrov, "Fresnel Formulas for the forced electromagnetic pulses and their application for optical to terahertz conversion in nonlinear crystals," *Physical Review Letters,* vol. 99, p. 203904, 2007.

[38] J. Hebling , K. L. Yeh, M. C. Hoffmann and K. A. Nelson, "High-Power THz generation, THz nonlinear optics and THz nonlinear spectroscopy," *IEEE Journal of Selected Topics in Quantum Electronics,* vol. 14, no. 2, pp. 345-353, 2008.